JACS
JOURNAL OF THE AMERICAN CHEMICAL SOCIETY
Article
pubs.acs.org/JACS

Semiring Chemistry of $Au_{25}(SR)_{18}$: Fragmentation Pathway and Catalytic Active site

Chunyan Liu,[†] Sisi Lin,[†] Yong Pei,*[,†] and Xiao Cheng Zeng[‡]

[†]Department of Chemistry, Key Laboratory of Environmentally Friendly Chemistry and Applications of Ministry of Education, Xiangtan University, Xiangtan, Hunan Province, P. R. China 411105

[‡]Department of Chemistry and Nebraska Center for Materials and Nanoscience, University of Nebraska—Lincoln, Lincoln, Nebraska 68588, United States

Supporting Information

ABSTRACT: The semiring chemistry of the $Au_{25}(SR)_{18}$, particularly its fragmentation mechanism and catalytic active site, is explored using density functional theory (DFT) calculations. Our calculations show that the magically stable fragmental cluster, $Au_{21}(SR)_{14}^-$, as detected in several mass spectrometry (MS) measurements of fragmentation of the $Au_{25}(SR)_{18}^-$, contains a quasi-icosahedral Au_{13}-core fully protected by four *-SR-Au-SR-* and two *-SR-Au-SR-Au-SR-* staple motifs. A stepwise fragmentation mechanism of the semiring staple motifs on the surface of $Au_{25}(SR)_{18}^-$ is proposed for the first time. Initially, the $Au_{25}(SR)_{18}^-$ transforms into a metastable structure with all staple motifs binding with two neighboring vertex Au-atoms of the Au-core upon energy uptake. Subsequently, a 'step-by-step' detachment and transfer of $[Au(SR)]_x$ (x = 1−4) units occurs, which leads to the formation of highly stable products including $Au_{21}(SR)_{14}^-$ and a cyclic $[Au(SR)]_4$ unit. The continued fragmentation of $Au_{21}(SR)_{14}^-$ to $Au_{17}(SR)_{10}^-$ is observed as well, which shows same stepwise fragmentation mechanism. The proposed mechanism well explains the favorable formation of $Au_{21}(SR)_{14}^-$ and $Au_{17}(SR)_{10}^-$ from $Au_{25}(SR)_{18}^-$ as observed from experimental abundance. Taking the $Au_{21}(SR)_{14}$ and its parent cluster $Au_{25}(SR)_{18}$ as the benchmark model systems, the catalytic active site of the thiolate protected gold clusters toward the styrene oxidation and the associated reaction mechanism are further investigated. We show that the Au atom in the staple motifs is the major active site for the styrene oxidation in presence of TBHP as oxidant or initiator. The Au atom in the staple motifs can change from Au(I) (bicoordinated) to Au(III) (tetracoordinated). The O_2 activation is achieved during this process.

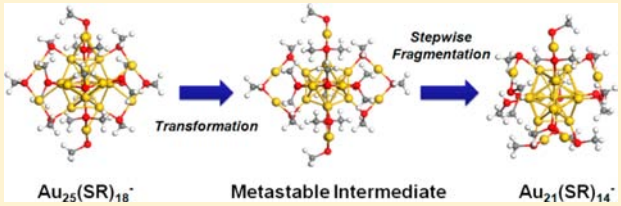

INTRODUCTION

Over the past decade, the thiolate group (−SR) protected gold nanoparticles (RS-AuNPs) have attracted intense research interest due to their unique electronic, catalytic, and optical properties.[1−6] A number of thiolated gold clusters with different compositions in the size range of 1−3 nm have been successfully synthesized and isolated by means of gold−thiol chemistry.[7−15] The small-sized thiolate protected gold clusters exhibit exceptional stability and sizable HOMO−LUMO gaps. However, the difficulty in crystallization of thiolate-protected gold clusters has greatly hindered the in-depth understanding of their structure−property relationship and slowed down their applications.

In recent years, breakthroughs have been made in total structure determination of RS-AuNP. The atomic structures of five thiolated gold clusters including $Au_{102}(p\text{-MBA})_{44}$ (where *p*MBA is *para*-mercapto benzoic acid, $SC_7O_2H_5$),[7] $Au_{25}(SCH_2CH_2Ph)_{18}^-$,[8,9k] $Au_{38}(SCH_2CH_2Ph)_{24}$,[9f] $Au_{36}(SPh\text{-}t\text{-}Ph)_{24}$,[9j] and $Au_{28}(SPh\text{-}t\text{-}Bu)_{20}$[9l] have been resolved successfully via single crystal X-ray diffraction (XRD). A novel picture of the gold−thiolate interactions in thiolate-protected gold clusters is established; i.e.. the −SR group is not merely adsorbed on the surface of an Au-core to form a single Au−S linkage, rather it can strongly disturb surface structures of the Au-cores and lead to the formation of novel gold−thiolate 'semiring' units (commonly named as semiring staple motif) on highly symmetric Au-cores.

The substantial progresses in the determination of accurate structures of thiolate-protected gold clusters allowed us to peer into the possible structural evolution rule and their size-dependent properties. A genetic structural rule that any thiolate protected gold cluster can be viewed as the combination of an intact, high-symmetric Au-core and a series of semiring staple motifs has been summarized.[16] The structure of the inner Au-core of any thiolate protected gold clusters is expected to evolve from the icosahedral atomic arrangements at smaller sizes to decahedral structures at larger ones.[7,9,16] This summarized structural rule has led to the structure prediction of various thiolate protected gold clusters, such as $Au_{12}(SR)_9^+$,[17a] $Au_{15}(SR)_{13}$,[17e,18b] $Au_{18}(SR)_{14}$,[18] $Au_{19}(SR)_{13}$,[17b] $Au_{20}(SR)_{16}$,[17c,19a] $Au_{24}(SR)_{20}$,[19b] $Au_{25}(SR)_{18}$,[20d] $Au_{38}(SR)_{24}$,[17d,19c,20a,b] $Au_{44}(SR)_{28}^{2-}$,[17f] and $Au_{144}(SR)_{60}$.[20c] Among these theoretical studies, the independent predictions

Received: May 17, 2013
Published: November 4, 2013

   dx.doi.org/10.1021/ja404957t | J. Am. Chem. Soc. 2013, 135, 18067−18079

of structure of $Au_{38}(SR)_{24}$ and $Au_{25}(SR)_{18}^-$ achieved great success that has been confirmed by later experiments. On the basis of the determined cluster composition and structures, a superatom-complex (SAC) model was proposed to explain their unique stabilities. According to the proposed SAC model, the number of free metal valence electron (n^*) of a thiolate protected cluster can be counted from $n^* = Nv_A - M - z$, where the Nv_A is the number of Au($6s^1$) electrons of the Au-core and M and z are the number of staple motifs and charge of cluster, respectively. On the basis of this model, the $Au_{25}(SR)_{18}^-$ and $Au_{102}(SR)_{44}$ have 8e and 58e contributed from the metallic Au-core, respectively, which satisfy the number of electrons that are needed to fill closed electron shell (spherical *jellium* model), explaining their magic stability.

In comparison to the recent progress of understanding the structural evolution and electronic structure of the Au-core, the chemistry of semiring staple motifs in the thiolate-protected gold clusters has been less addressed. To date, different kinds of semiring staple motifs such as the monomeric (*-SR-Au-SR-*), dimeric (*-SR-Au-SR-Au-SR-*), trimeric (*-SR-Au-SR-Au-SR-Au-SR-*) and even pentameric (*-SR-Au-SR-Au-SR-Au-SR-Au-SR-Au-SR-*) staple motif have been discovered or proposed.[7−9,16] However, the chemical properties of semiring staple motifs in these yet small but robust clusters, i.e., their fragmentation mechanism in mass spectroscopy (MS) and possible role in the catalytic reactions, are not well studied.

In this article, we report a theoretical study of the fragmentation pathway and catalytic active site of a well-known thiolate protected gold cluster, i.e., $Au_{25}(SR)_{18}^-$, so as to explore the semiring chemistry of thiolate protected gold clusters. The concept of the 'semiring chemistry' was first proposed by Murray et al. during the studies of structure, optical properties and MS-fragmentation of the $Au_{25}(SR)_{18}^-$.[1g] In the $Au_{25}(SR)_{18}^-$, a quasi-icosahedron Au_{13}-core is wrapped by six dimeric *-SR-Au-SR-Au-SR-* semiring staple motifs. Upon the energy-uptake in MS, the $Au_{25}(SR)_{18}^-$ exhibits several interesting fragmentation patterns. The small fragments such as Au(SR), $Au_2(SR)_3$ and $[Au(SR)]_4$, as well as a series of fragment clusters $Au_mL_n^-$ (L = S or SR), have been found in ion mobility mass spectrometry (IM-MS), electrospray ionization (ESI), matrix-assisted laser desorption/ionization (MALDI), and fast atom bombardment (FAB) mass spectrometry.[21−28] Among various fragmented clusters, the $Au_{21}(SR)_{14}^-$ has been detected as a highly stable one (denoted as a magic number cluster), which is typically signified by an intense shoulder peak of $Au_{25}(SR)_{18}^-$. Dass et al. showed that most dominant and largest fragments of $Au_{25}(SR)_{18}^-$ detected in the IM-MS are $Au_{21}(SR)_{14}^{+,-}$ and $Au_{17}(SR)_{10}^{+,-}$ with electron counts of 8 and 6 in negative and positive mode, respectively.[23] In the FAB-MS of $Au_{25}(SR)_{18}^-$, the serial loss of Au(SR) unit was observed.[21] Notably, the $Au_{21}(SR)_{14}^-$ resulting from the loss of an $[Au(SR)]_4$ unit was also identified as the magically stable product. The prevailing loss of $[Au(SR)]_4$ unit is observed in MALDI-MS fragmentation of doped Au_{25} cluster as well, e.g., $Pd_1Au_{24}(SR)_{18} \rightarrow Pd_1Au_{20}(SR)_{14} + [Au(SR)]_4$.[27] However, the pathway for the formation of such a popular species during the MS fragmentation is not well understood. Although a recent IM-MS experiment has clearly shown that the stepped fragmentation of $Au_{25}(SR)_{18}^-$ starts from the semiring staple first then to the Au_{13}-core with the increase of the collision energies,[23] it is difficult to imagine a *one*-step loss of the $[Au(SR)]_4$ unit from the well-established structure of $Au_{25}(SR)_{18}^-$, given the uniformly distributed *-SR-Au-SR-Au-SR-* semiring staple motifs on the Au core. As a comparison, the structures of the $Au_mS_n^-$ fragmentation clusters caused by the fragmentation of the inner Au_{13}-core of $Au_{25}(SR)_{18}^-$ at higher collision energies[23] were predicted recently via DFT calculations.[29,30] Remarkably, the magic-number clusters such as $Au_6S_4^-$, $Au_9S_5^-$, $Au_9S_6^-$, $Au_{10}S_6^-$, $Au_{11}S_6^-$, $Au_{12}S_8^-$ and $Au_{13}S_8^-$ are found to possess hollow-polyhedron structures such as quasi-tetrahedron, pyramidal, quasi-triangular prism, or quasi-cuboctahedron with or without an encapsulated Au atom.[29] Moreover, the core-in-cage structures are also predicted for $Au_{25}S_{12}^-$, $Au_{23}S_{11}^-$ and $Au_{27}S_{13}^-$ where the Au core is encapsulated in a series of Au_mS_n cages composed of S−Au−S edges.[30]

Recently, Lopez-Acevedo et al. theoretically investigated the relative stabilities of fragmentation species from $Au_{25}(SR)_{18}^-$, including $Au_{24}(SR)_{17}^-$ plus a Au(SR) unit, $Au_{23}(SR)_{16}^-$ plus a $[Au(SR)]_2$ unit, $Au_{22}(SR)_{15}^-$ plus a $[Au(SR)]_3$ unit, and $Au_{21}(SR)_{14}^-$ plus a $[Au(SR)]_4$ unit.[31] It was found that among various fragmental species the combination of $Au_{21}(SR)_{14}^-$ and a cyclic $[Au(SR)]_4$ gives rise to the lowest energy. The formation of the $Au_{21}(SR)_{14}^-$ fragmentation product was ascribed to a thermodynamics favorable process. However, detailed fragmentation pathway from $Au_{25}(SR)_{18}^-$ to $Au_{21}(SR)_{14}^-$ and the lowest-energy structure of $Au_{21}(SR)_{14}^-$ remain elusive, although some experimental studies suggested the rearrangement of the semiring staple motifs may happen prior to the dissociation of a $[Au(SR)]_4$ unit from $Au_{25}(SR)_{18}^-$.[23,24,28] A better understanding of the atomic structure and formation mechanism of $Au_{21}(SR)_{14}^-$ will undoubtedly provide valuable information on the rearrangement and fragmentation process of the semiring staple motifs on $Au_{25}(SR)_{18}^-$, hence a deeper insight into the structure and properties of the cluster. Furthermore, the determination of structures of the fragmental clusters can also provide clues on the structure of their parent cluster in MS, so as to conjecture the structure of some unresolved thiolate protected gold clusters.[21−28] Herein, the structure of $Au_{21}(SR)_{14}^-$ cluster is studied using our recently developed 'divide-and-protect' scheme combined with DFT optimization.[19b] A fragmentation pathway of $Au_{25}(SR)_{18}^-$ that can be described by a stepwise mechanism involving an initial transformation of $Au_{25}(SR)_{18}^-$ into a metastable structure with all staple motifs binding with two neighboring vertex Au-atoms of the Au-core and subsequent 'step-by-step' detachment of $[Au(SR)]_x$ (x = 1−4) units is proposed for the first time. This mechanism provides an explanation of the apparent abundance of $Au_{21}(SR)_{14}^-$ cluster detected in the several MS experiments.

On basis of the resolved cluster structure of $Au_{21}(SR)_{14}^-$ and its parent Au_{25} cluster, the reaction mechanism toward styrene oxidation on both neutral $Au_{25}(SR)_{18}$ and $Au_{21}(SR)_{14}$ is further studied to explore the active site and size-dependent catalytic activities of thiolate protected gold clusters. It is found that the common catalytic active site on the thiolate-protected gold clusters toward the styrene oxidation is the Au(I) atom in the semiring staple motifs rather than the metallic Au-core proposed previously, irrespective of the length of the semiring staple motifs and cluster composition. The present studies of the fragmentation mechanism and catalytic active sites of $Au_{25}(SR)_{18}^-$ and $Au_{21}(SR)_{14}^-$ provide new insights into the rich chemistry of the semiring staple motifs on the thiolate protected gold clusters.

The paper is organized in two parts: (1) A study of the fragmentation mechanism of semiring staple motifs of

dx.doi.org/10.1021/ja404957t | J. Am. Chem. Soc. 2013, 135, 18067−18079

$Au_{25}(SR)_{18}^-$is reported. To this end, the lowest-energy structure of the anionic and neutral $Au_{21}(SR)_{14}$ clusters is first determined via our recent developed force-field based 'divide-and-protect' approach. With the newly determined structure of $Au_{21}(SR)_{14}^-$, the detailed fragmentation mechanism of the semiring staple motifs on its parent cluster $Au_{25}(SR)_{18}^-$ is systematically investigated. Moreover, the further fragmentation of $Au_{21}(SR)_{14}^-$ to $Au_{17}(SR)_{10}^-$ is examined as well. (2) The role of the semiring staple motifs played in the catalytic oxidation of styrene is investigated on the basis of the resolved structure of $Au_{21}(SR)_{14}$ and its parent cluster $Au_{25}(SR)_{18}$.

■ COMPUTATIONAL METHOD AND DETAILS

DFT optimizations of different $Au_{21}(SR)_{14}$ isomers are performed using the generalized gradient approximation (GGA) with the Perdew-Burke-Ernzerhof (PBE) functional[32] or meta-hybrid GGA functional TPSS[33] and M06.[34] With the Dmol^3 package, the *d*-polarization included basis set (DND) is used for C, H, S elements.[35] The DFT Semicore Pseudopot (DSPP) approximation with some degree of relativistic corrections into the core is used for the Au element. For the 16 lowest-lying isomers obtained from PBE/DND calculations, we reoptimize their structures using the higher-level triple-ζ polarized (TZP) basis set with inclusion of scalar relativistic effect via zeroth-order regular approximation (ZORA) implemented in the ADF package[36] and the functional TPSS, as well as the M06 functional with the basis sets LANL2DZ for Au and 6-31G(d) for C, H, and S atoms, implemented in the Gaussian09 package.[37] The time-dependent TDDFT computation of optical absorption spectra is performed using the correct exchange functional of Van Leeuwen and Baerends (LB94) functional[38] combined with TZP basis set, implemented in the ADF package, which has been shown to well reproduce the feature of optical curve of $Au_{25}(SR)_{18}^-$.[39] The TDDFT calculations evaluate the lowest 230 singlet-to-singlet excitation energies for $Au_{21}(SR)_{14}$. For the cluster species having unpaired electrons, the spin-polarized DFT calculations are used. The Born−Oppenheimer molecular dynamics (BOMD) simulations are also performed based on the PBE functional with a mixed Gaussian and plane-wave basis,[40] i.e., DZP-MOLOPT basis set implemented in the CP2K code.[41] For the plane-wave wave functions, the energy cutoff is set to be 80 Ry. The interaction between the valence electrons and the atomic cores is described using the Goedecker-Teter-Hutter (GTH) pseudopotential.[42] The constant-temperature and constant-volume (NVT) ensemble is adopted for the BOMD simulation.

■ RESULTS AND DISCUSSION

1. Structure of the $Au_{21}(SR)_{14}$. Before discussing the fragmentation mechanism of $Au_{25}(SR)_{18}^-$ to $Au_{21}(SR)_{14}^-$, we first attempt to determine the lowest-energy structure of the magically stable product $Au_{21}(SR)_{14}^-$. The search of the most stable structure of $Au_{21}(SR)_{14}^-$ clusters is based on our recently proposed force-field based 'divide-and-protect' approach.[19b] Although numerous global-optimization methods for atomic clusters have been developed,[43−46] they are inefficient for the thiolate-protected Au nanoclusters due to the complex interaction between Au and −SR groups and demanding computational costs. With the known atomic structures of $Au_{25}(SR)_{18}^-$, $Au_{38}(SR)_{24}$, and $Au_{102}(SR)_{44}$, certain intrinsic structural rules have been established, which are indispensable to construct sensible isomer structures and greatly narrow down the scope of global-minimum search.[16] One of the most heuristic rules is the 'divide-and-protect' concept, which describes the thiolate-protected Au nanoparticles as an ordered Au core covered by a number of capping units with different lengths, $RS(AuSR)_x$. Once the chemical formula of clusters is determined, a structural formula can be proposed to characterize the clusters with the core/capping unit divisions $[Au]_{a+a'}[Au(SR)_2]_b[Au_2(SR)_3]_c$, etc., where a' is the number of outer Au-atom of Au-core that are passivated by the terminal −SR group of the staple motifs, and a is the number of Au-atom in the inner Au-core that do not contact directly with the staple motifs, b and c are the number of monomeric and dimeric staple motifs, respectively.

For $Au_{21}(SR)_{14}^-$, only the monomeric and dimeric staple motifs are considered in the structural formula as its Au/SR ratio (1.5) is very close to that of $Au_{38}(SR)_{24}$ (1.58), denoted as $[Au]_{a+a'}[Au(SR)_2]_b[Au_2(SR)_3]_c$. The constraint that the total number of the S-terminals of the semiring staple motifs must equal the number of the Au atom on the core surface can significantly reduce possible structural divisions.[16,19] With these constraints, the parameters a, a', b and c are related with one another via the following three equations: $a + a' + b + 2c = 21$, $2b + 3c = 14$, and $a' = 2(b + c)$. Next, two subgroups of parameters can be determined from these constraints: the division $[Au]_{1+12}[Au(SR)_2]_4[Au_2(SR)_3]_2$ and $[Au]_{2+10}[Au(SR)_2]_1[Au_2(SR)_3]_4$. As the structures of semiring protecting units $Au(SR)_2$ and $Au_2(SR)_3$ are already known, the task is simplified as to the search of a proper Au-core covered by certain numbers of $Au(SR)_2$ and $Au_2(SR)_3$ staple motifs.

We consider that the Au cores in the clusters tend to adopt highly symmetric structures based on the observation from the several structurally known thiolate-protected gold clusters. We then use the Sutton-Chen potential[47] combined with the basin-hopping method[46] to generate a database of Au-core structures (not the global minimum) as discussed in our previous work.[19b] With the structural database, we can select all symmetric cores as candidates for testing structure assembling and performing DFT geometric optimization. The selection of the Sutton-Chen potential is validated from three independent benchmark searches of the Au_{13}, Au_{23}, and Au_{79} cores of the $Au_{25}(SR)_{18}^-$, $Au_{38}(SR)_{24}$, and $Au_{102}(SR)_{44}$ clusters, respectively. The realistic Au-core structures are all found within the corresponding database of Au-cores.

On the basis of the $[Au]_{1+12}[Au(SR)_2]_4[Au_2(SR)_3]_2$ or $[Au]_{2+10}[Au(SR)_2]_1[Au_2(SR)_3]_4$ divisions, we have generated databases for the Au_{12}- and Au_{13}-core structures and collected those close-packing structures with high symmetries. For the Au_{13} core, two structures (Core 1 and Core 2) are identified as shown in Figure 1. For the Au_{12} core, again two structures are identified with one (Core 3) being viewed as a vertex-truncated icosahedron and another (Core 4) having the D_{2d} symmetry. In addition, we have considered several other Au cores (e.g., Core 5 and Core 6 in Figure 1) and made some subtle adjustments on their structures so that they can be more suitable for the next-step core/motif assembly.

Once the core structures are collected, the next step is to cover the cores with appropriate staple motifs for assembling various candidate clusters. In view of the division $[Au]_{1+12}[Au(SR)_2]_4[Au_2(SR)_3]_2$, we first consider replacing four dimeric capping units on the prototype $Au_{25}(SR)_{18}^-$ with the shorter monomeric ones. This replacement leads to two reasonable configurations where the two longer semiring staple motifs are either adjacent or opposite to one another. Note that two similar structures of $Au_{21}(SR)_{14}^-$ with the replacement of four semiring dimeric staple motifs by reduced monomeric ones have been reported recently,[31] which are proven to be higher energy isomers (labeled as **Iso7** and **Iso8** in Supporting Information Table S1). A prominent structural modification

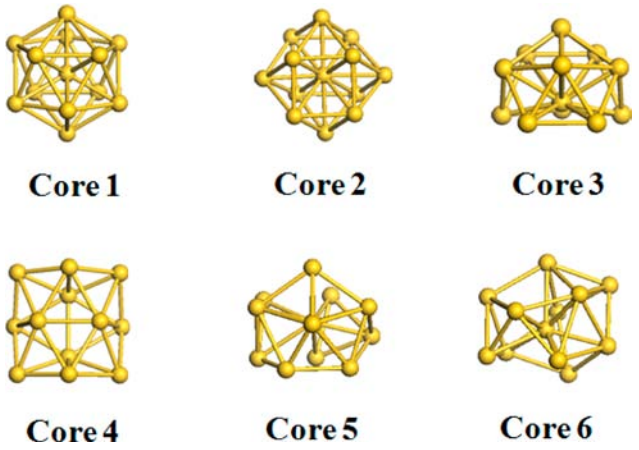

Figure 1. Six types of Au-core selected in the 'divide-and-protect' scheme. Core 1 and Core 2 belong to the Au_{13} core, and others belong to the Au_{12} core.

due to the replacement of two dimeric staple motifs by monomeric units is that the reduced monomeric motifs are initially bonded to diagonal triangular vertexes to wrap around two adjacent faces of the icosahedral core. After the geometric optimizations, the monomeric staple motifs finally turn into covering only an edge on the surface, i.e., bonded with a pair of adjacent Au-vertexes. Except for these two structures, the same phenomena are also observed from the optimized results of several other structures that contain one or more initial monomeric motifs bonded to diagonal vertexes. As a result, we recognize that the bonding of the shorter staple motifs to the diagonal gold atoms on the core can cause the distance between Au atoms (in the staple motifs) and another two Au atoms (in the wrapped faces) to be too close, leading to increased tensions and large structural deformation due to the intrinsic high-curvature of the icosahedral Au_{13} core.

To obtain more reasonable starting configurations, we have examined a variety of configurations of staple motifs for the division $[Au]_{1+12}[Au(SR)_2]_4[Au_2(SR)_3]_2$, including possible permutations of the two Au-core atoms not directly bonded with S-terminals in the division of $[Au]_{2+10}[Au(SR)_2]_1[Au_2(SR)_3]_4$. On the basis of the two divisions, over *80 isomer structures* are constructed and then optimized at the level of PBE/DND, where all the −R groups are simplified as the methyl group (denoted as Me in the discussions below) for reducing computing cost. The computed relative energies at PBE/DND level of isomers are all illustrated in Figure 2. One can see that isomers of $Au_{21}(SMe)_{14}^-$ with an icosahedral Au_{13}-core possess relative lower energies. But for the neutral cluster, the PBE/DND optimization predicts that the isomers with an Au_{12} core have lower energies than those with the Au_{13}-core. To further confirm the energy order of low-energy structures of $Au_{21}(SMe)_{14}^-$, we have reoptimized 16 isomers with relatively lower energies at the level of PBE/TZP using the ADF package (see Figure 2 and Figure S1 in the Supporting Informaion). Here, the PBE/TZP calculations indicate isomers **Iso1**−**Iso8** (see Figure 3, Table S1 and Figure S1 in the Supporting Information) containing a quasi-icosahedron Au_{13} core are more stable than other low-lying isomers with other types of Au-core or divisions (see **Iso9**−**Iso16**). At the same time, the meta-GGA TPSS and M06 functionals combined with the LANL2DZ basis set (for Au) and 6-31(G) basis set (for S, C, H), as well as the PBE with larger SDD basis set and more

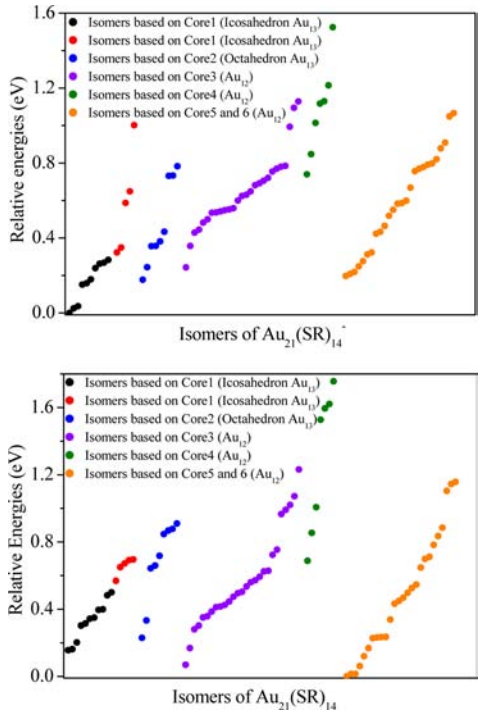

Figure 2. Relative energies of isomers of (top) anionic and (bottom) neutral $Au_{21}(SMe)_{14}$ at the PBE/DND level of theory. Black and red points represent the relative energies of isomers based on the icosahedral Au_{13}-core (Core 1). Red points represent the relative energies of isomers based on icosahedral Au_{13}-core with the monomeric staple motifs bonded to a pair of diagonal vertexes; blue points represent the relative energies of isomers based on Core 2; violet points represent the relative energies of isomers based on Core 3; olive points represent the relative energies of isomers based on Core 4; and orange points represent the relative energies of isomers based on other Au_{12}-core (Core 5 and Core 6).

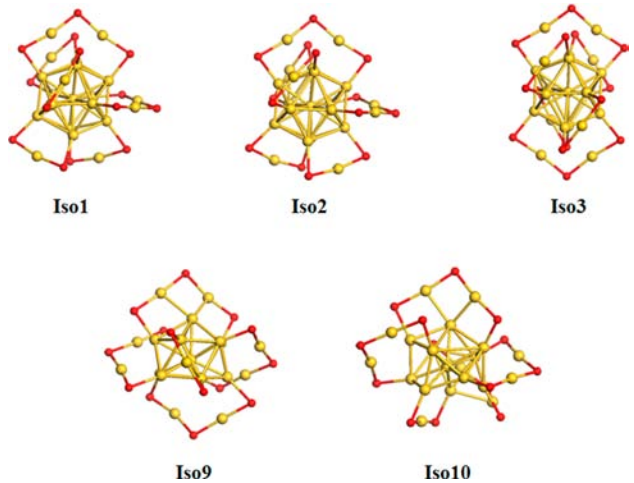

Figure 3. Optimized structures of **Iso1**−**3** and **Iso9**−**10** for $Au_{21}(SMe)_{14}^-$. The methyl groups are removed for clarity. The Au and S atoms are represented by yellow and red colors, respectively. The **Iso1**−**3** contain Core 1 with the division of $[Au]_{1+12}[Au(SR)_2]_4[Au_2(SR)_3]_2$, and **Iso9**−**10** contain Core 3 and Core 5, respectively, with the division of $[Au]_{2+10}[Au(SR)_2]_1[Au_2(SR)_3]_4$.

expensive MP2[48] calculations, are also used to evaluate relative stabilities of the low-lying isomers. Computations with the TPSS and M06 functionals indicate that the **Iso1**−**8** with an

dx.doi.org/10.1021/ja404957t | J. Am. Chem. Soc. 2013, 135, 18067−18079

icosahedral Au_{13} core possess much lower energy than **Iso9**−**Iso16** with the Au_{12} core for anionic $Au_{21}(SMe)_{14}$, although the energy rankings among isomers predicted by TPSS and M06 are a little inconsistent (see Table 1 and Table S1 in the Supporting Information). The more accurate MP2/LANL2DZ/6-31G* calculations show that the **Iso1** with the dimeric staple motifs wrapping across two triangular Au_3-units are much more stable by 1.76 and 1.85 eV than previously proposed isomer structures[31] with the dimeric staple motifs dangling on the Au-core (denoted as **Iso7** and **Iso8**, respectively, see Table S1 in the Supporting Information), which further confirms the present structural predictions.

Table 1. Relative Energies (eV) of Iso1−3 and Iso9−10 of Anionic $Au_{21}(SMe)_{14}$ at Three Different Levels of Theory[a]

isomers	TPSS[b]	M06[b]	PBE[c]	H−L Gap[d]	core type
Iso1	0.000	0.000	0.000	1.254	Core 1
Iso2	0.003	0.092	−0.005	1.266	Core 1
Iso3	0.074	0.307	0.125	1.162	Core 1
Iso9	0.496	0.521	0.241	1.299	Core 3
Iso10	0.639	0.620	0.200	0.837	Core 5

[a]H−L Gap is the HOMO−LUMO gap of the isomer. The core types correspond to those listed in Figure 1. The complete data of top 16 lowest-energy isomers and their structures are given in the Supporting Information Table S1. [b]The basis used for the computations is LANL2DZ for Au and 6-31G(d) for C, H, S elements, respectively. [c]The basis set is TZP with ZORA approximation. [d]The H−L gaps are computed at the PBE/TZP level of theory.

Furthermore, we carry out identical steps to search the most stable isomer structure of the neutral cluster. Previous experimental studies on $Au_{25}(SR)_{18}^-$ indicate the negative charge only slightly affects the structures of core and staple motifs.[49] Here, our extensive calculations suggest that the lowest-energy structure of neutral $Au_{21}(SMe)_{14}$ predicted from both TPSS and M06 functionals is the same as that of the anionic species, e.g., **Iso1** (Figure 3), except very slight differences in the corresponding bond lengths and bond angles. Note that the PBE/TZP computation predicts a reverse ranking of stabilities of neutral isomers, compared to TPSS and M06 functional, which suggests isomers containing a vertex-truncated Au_{12}-core are slightly more stable than those containing a quasi-icosahedron Au_{13}-core. Herein, we adopt the energy rankings predicted from the meta-GGA functionals. Although the neutral and anionic clusters possess similar configurations in the lowest-energy structure, there is a disparity in the energy ranking that the isomers of anionic clusters with the division $[Au]_{1+12}[Au(SR)_2]_4[Au_2(SR)_3]_2$ generally outrank other divisions, but for the neutral cluster this superiority is not so straightforward due to the crossover in the energy rankings for isomers containing different classes of cores. Relative energies of neutral isomers based on different approaches are summarized in the Table 2 and Table S2 (in the Supporting Information).

The newly predicted lowest-energy structure of $Au_{21}(SR)_{14}$ exhibits several interesting connections with its parent cluster. As shown in Tables 1 and 2, the **Iso1** (see Figure 3) with a quasi-icosaheron Au_{13}-core is the leading isomer candidate for the global minimum of $Au_{21}(SMe)_{14}$ in both neutral and anionic states. Moreover, according to the relative energies computed from the TPSS and M06 functionals, all the top three lowest-lying structures (**Iso1**−**Iso3**) entail similar

Table 2. Relative Energies (eV) of Iso1−3 and Iso9−10 of Neutral $Au_{21}(SMe)_{14}$ at Three Different Levels of Theory[a]

isomers	TPSS[b]	M06[b]	PBE[c]	core type
Iso1	0.000	0.000	0.000	Core 1
Iso2	0.023	0.123	0.023	Core 1
Iso3	0.084	0.216	0.151	Core 1
Iso9	0.453	0.488	0.315	Core 3
Iso10	0.270	0.256	−0.136	Core 5

[a]The core types correspond to those listed in Figure 1. The complete data of top 16 lowest-energy isomers and their structures are given in the Supporting Information Table S2. [b]The basis set used for the computations is LANL2DZ for Au, and 6-31G(d) for C, H, S elements. [c]The basis set is TZP with ZORA approximation.

structures, indicating that the icosahedral Au_{13}-core is energetically the most favorable for the $Au_{21}(SMe)_{14}$. As a result, the icosahedral Au_{13}-core is expected to be intact during the fragmentation $Au_{25}(SMe)_{18}^- \rightarrow Au_{21}(SMe)_{14}^- + [Au(SMe)]_4$, which is in agreement with recent MS studies.[23] However, despite of the robustness of icosahedra Au_{13}-core in $Au_{21}(SMe)_{14}^-$, the four shorter motifs should not be treated just as a simple replacement of the original dimeric semiring motifs by the monomeric motifs since the surface tension incurred by the very short distance between the Au atoms in the shorter staples and the Au atoms on the core surface may lead to significant rearrangement of surface motifs to compensate the unfavorable surface strain. In the **Iso1**, the four capping monomeric staple motifs are bonded with pairs of adjacent Au atoms on the core surface, where the Au−Au bond lengths (3.0−3.4 Å) between two adjacent Au atoms are slightly longer than those in $Au_{25}(SMe)_{18}^-$ (2.7−3.0 Å). The dimeric staple motifs remain adjacent and perpendicular to each other similar to the interfacial structure of $Au_{25}(SMe)_{18}^-$. The uneven distribution and diversity of the staple motifs eventually induce distortion of the Au-core structure and hence make the whole cluster lose the symmetry.

On the other hand, the $Au_{21}(SR)_{14}^-$ has a valence electron shell of 8*e* according to the electron-counting rule, similar to the parent Au_{25} cluster.[50] It is thus of interesting to compare the electronic structure and optical absorption properties of two clusters. Figure S1 displays the simulated UV−vis absorption spectra of $Au_{21}(SMe)_{14}$ clusters in both neutral and anionic states. The component of Kohn−Sham orbitals and the transition corresponding to different absorption peaks of the lowest energy structure of $Au_{21}(SMe)_{14}^-$ (**Iso1**) are examined as well. It is found that the optical absorption curve of **Iso1** exhibits very similar feature peaks to those of $Au_{25}(SMe)_{18}^-$[9k]. The two observed feature peaks at 1.65 and 2.3 eV of Au_{21} cluster are contributed from the electronic transition from the HOMO to LUMO and the transitions from lower occupied orbital to unoccupied orbital, respectively, as shown in Figure S1. The Mulliken charge population analysis indicates that the HOMO, HOMO-1, HOMO-2 and the unoccupied orbitals of $Au_{21}(SMe)_{14}^-$ are mainly composed of 6 sp atomic orbitals of gold (summarized as the Au-sp band), and the lower energy orbitals such as HOMO-4, HOMO-5 stem from the Au-5d[10] atomic orbitals of gold (denoted as the d-band), similar to the electronic structure of $Au_{25}(SMe)_{18}^-$. However, owing to the low symmetry of Au_{21} cluster, both HOMO and LUMO are no longer degenerate, as opposed to the triply degenerated HOMO and doubly degenerated LUMO for the $Au_{25}(SMe)_{18}^-$.[9k] Furthermore, the displayed optical

dx.doi.org/10.1021/ja404957t | J. Am. Chem. Soc. 2013, 135, 18067−18079

curves of Au_{21} cluster in different structural divisions such as $[Au]_{1+12}[Au(SR)_2]_4[Au_2(SR)_3]_2$ and $[Au]_{2+10}[Au(SR)_2]_1[Au_2(SR)_3]_4$ (**Iso1**−**Iso16**) also allow one to further distinguish the structure and properties of various isomers.

2. Fragmentation Mechanism of the Semiring Staple Motifs on $Au_{25}(SR)_{18}^-$. Although the magic stability of $Au_{21}(SR)_{14}^-$ has been confirmed by several MS experiments, the detailed mechanism of the formation of this magic stable cluster via the fragmentation of $Au_{25}(SR)_{18}^-$ remains elusive. Some attempts have been made to prepare the Au_{21} cluster via the heating of $Au_{25}(SR)_{18}^-$ but have been unsuccessful.[51] Thus far, the $Au_{21}(SR)_{14}^-$ can be only observed in some high-energy MS. Dass et al. found that with the increase of the collision energy, the semiring staple motifs on the $Au_{25}(SR)_{18}^-$ are first fragmented, then followed by the Au_{13}-core.[23] The $Au_{21}(SR)_{14}^-$ represents the dominant product during the course of fragmentation of the surface semiring staple motifs.[23] It was therefore proposed that the formation of $Au_{21}(SR)_{14}^-$ from the $Au_{25}(SR)_{18}^-$ might involve a series of rearrangement of the outer staple motifs and cleavages of interfacial Au−S bonds.[23,24,28]

Here, we first attempt to simulate the initial stage of the fragmentation of $Au_{25}(SMe)_{18}^-$ (the −R is simplified by methyl group) using ab initio Born-Oppenheimer molecular dynamics (BOMD). The BOMD simulation is performed in the NVT ensemble with the temperature controlled at 1000 K to simulate the structural evolution of $Au_{25}(SMe)_{18}^-$ in the MS (corresponding to impose ∼14.9 eV energy on the $Au_{25}(SMe)_{18}^-$ cluster) to mimic the high energy state of the cluster during the energy-uptake in the MS. The BOMD simulation lasts 7 ps with the time-step is 1 fs. The potential energy evolution of the system is shown in Figure 4a. By examining the BOMD trajectory, we find that neither the Au-core nor the staple motifs on the cluster surface is fragmented during the 7 ps simulation. However, a major structural transition of $Au_{25}(SMe)_{18}^-$ is clearly seen such that the arrangement of staple motifs is dramatically changed after ∼3.5 ps. As shown in Figure 4a, the quenched structure from an intermediate structure before ∼3.5 ps shows that the structure of $Au_{25}(SMe)_{18}^-$ is nearly the same as the initial structure. After 3.5 ps, a major structural transition of the cluster occurs that the staple motifs on $Au_{25}(SMe)_{18}^-$ rearrange dramatically. The dimeric staple motifs no longer bind to diagonal Au-vertexes to wrap two adjacent faces of the icosahedral Au_{13}-core. Instead, they bind to two neighboring Au-atoms to form a new type of interfacial structure within ∼3.5 ps, which eventually leads to the formation of a new interfacial structure.

In Figure 4b, we show the energy difference (at PBE/DND level) between the starting structure of $Au_{25}(SMe)_{18}^-$ and a new structural pattern due to the energy uptake. The new structure (denoted as **Au_{25}−Iso1**) with the staple motifs binding to two neighboring Au-vertexes is higher in energy by 0.83 eV than the original crystal structure. The energy pathway for the structural transition from the crystal structure of $Au_{25}(SMe)_{18}^-$ to **Au_{25}−Iso1** is also computed. It is found that the transition state between two structures contains an octahedron Au_{13}-core. The reverse structural transition from the **Au_{25}−Iso1** to the crystal structure of $Au_{25}(SMe)_{18}^-$ is separated by a barrier of 0.47 eV (Figure 4b), indicating that the newly formed metastable structure can exist as an intermediate for further fragmentation.

The **Au_{25}−Iso1** exhibits very similar structural pattern of staple motifs to the **Iso1** of $Au_{21}(SMe)_{14}^-$, namely, the staple

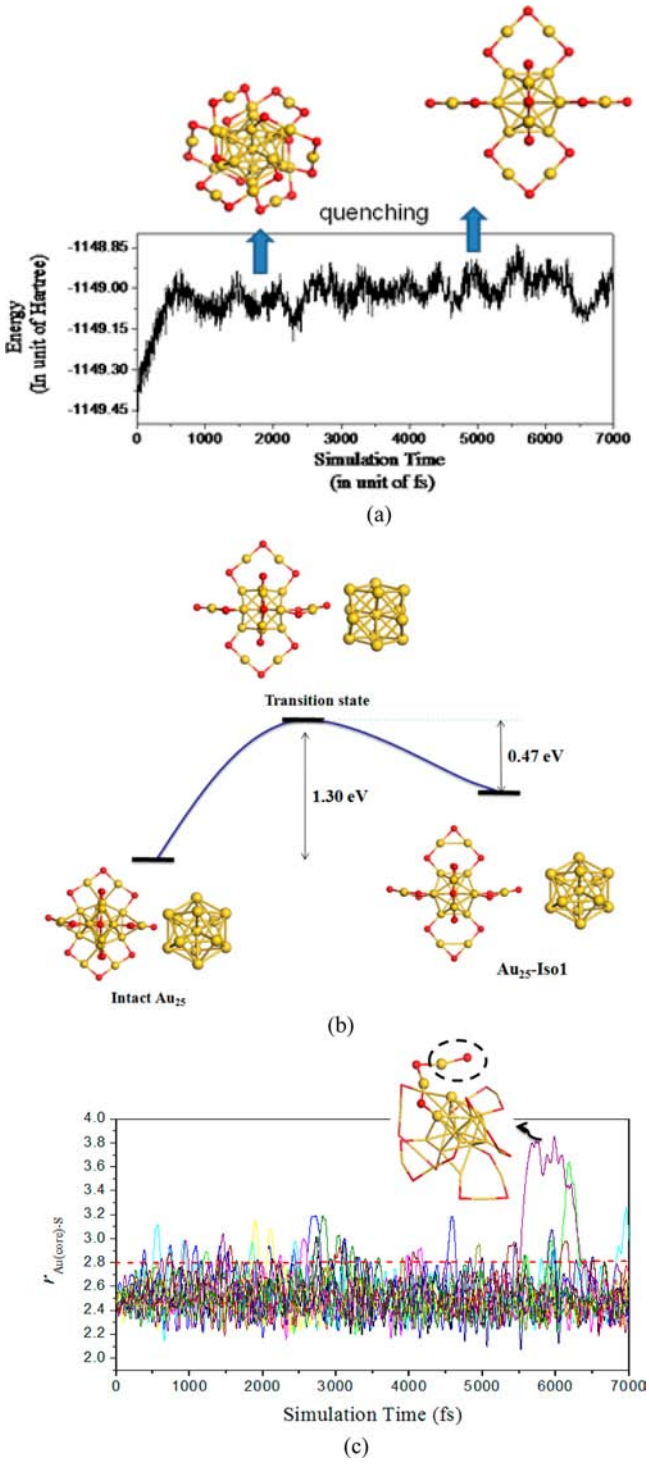

Figure 4. (a) Potential energy evolution during the 7 ps BOMD simulation. (b) The energy curve for characterizing the structural transition between the intact $Au_{25}(SMe)_{18}^-$ and a new structural pattern **Au_{25}−Iso1**. The methyl groups are omitted for clarity. (c) The time-evolution of bond lengths of Au-core atoms and the S-terminal of staple motifs (totally 12 interfacial Au(core)−S bonds are considered).

motifs are bound to two neighboring vertex Au-atoms. We speculate that the formation of $Au_{21}(SMe)_{14}^-$ may go through loss of a series of $Au_x(SMe)_y$ units from the semiring staple motifs on **Au_{25}−Iso1**. To confirm this speculation, we first examine the fluctuation of bond length between the S-terminal of the staple motif and the Au-core during the BOMD

dx.doi.org/10.1021/ja404957t | J. Am. Chem. Soc. 2013, 135, 18067−18079

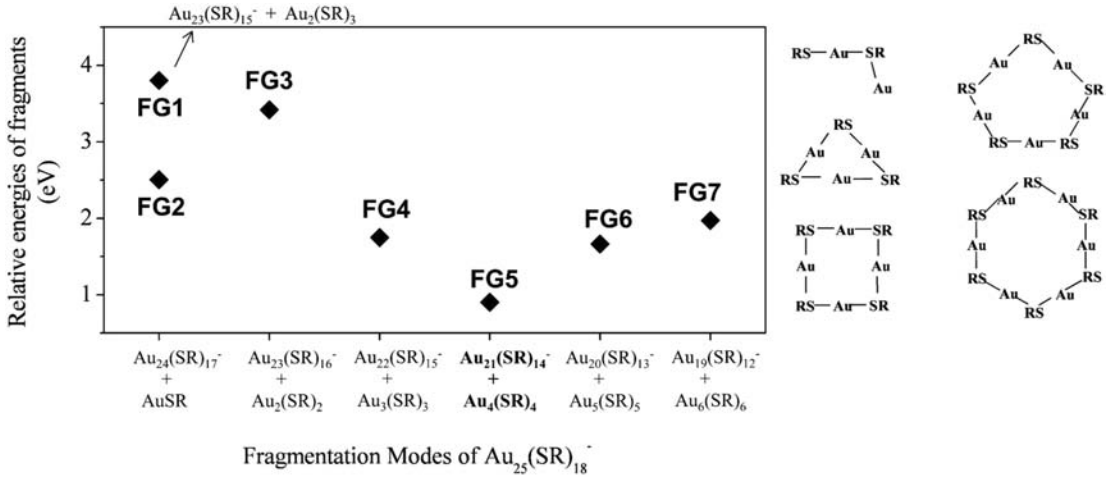

Figure 5. Relative energies of fragmentation products from $Au_{25}(SR)_{18}^-$ in different fragmentation modes. The −R group is simplified into methyl group in energy calculations. **FG1**− 7 denote the fragment species of $Au_{23}(SR)_{15}^-$ plus $Au_2(SR)_3$ unit (**FG1**); $Au_{24}(SR)_{17}^-$ plus $[Au(SR)]$ unit (**FG2**); $Au_{23}(SR)_{16}^-$ plus $[Au(SR)]_2$ unit (**FG3**); $Au_{22}(SR)_{15}^-$ plus $[Au(SR)]_3$ unit (**FG4**); and $Au_{21}(SR)_{14}^-$ plus $[Au(SR)]_4$ unit (**FG5**). The right five structural schemes denote the structure of fragmented species $[Au(SR)]_x$ (x = 2−6) used in energy calculations.

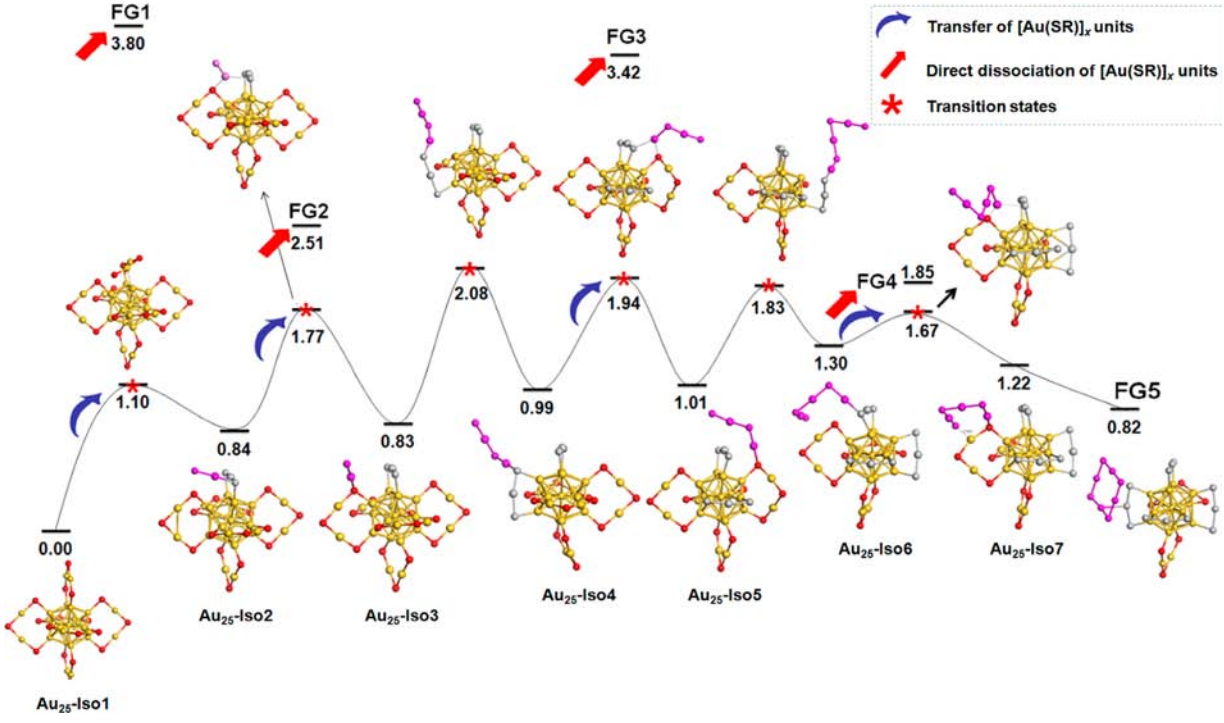

Figure 6. The sequential release of $[Au(SR)]_x$ (x = 1−4) unit from the $Au_{25}(SR)_{18}^-$, where the −R group is simplified into methyl group. The blue arrow indicates a low energy pathway and the red arrow shows a high energy pathway. The **FG1** to **FG5** correspond to the fragment species described in Figure 5. The energy is in unit of eV. The methyl groups in the clusters are omitted for clarity. The atoms colored in pink denote the detached and transferred $[Au(SR)]_x$ units. The atoms colored in gray denote the formed monomeric staple motifs. Atoms in yellow and red are Au and S atoms, respectively.

simulation. Figure 4c clearly shows that the bond length of the interfacial Au(core)−S bond fluctuates significantly. In certain time widows (e.g., 5.5−6.0 ps), the Au(core)−S bond length even reaches 3.6 Å, much longer than that in the unperturbed cluster (about 2.40−2.45 Å). A snapshot of the cluster at 6.0 ps is also displayed in Figure 4c, where it shows that one S-terminal of staple motif detaches from the cluster surface. Here, we define a critical length of 2.80 Å for the Au(core)−S bond, beyond which the Au(core)−S bond is considered to be dissociated. As shown in Figure 4c, in several simulation stages the bond length of Au(core)−S exceeds the critical length. A prominent effect due to the elongated Au(core)−S bond length is the likely the reason for of the detachment of $Au_x(SMe)_y$ units from the staple motifs. Hence, the fragmentation of $Au_{25}(SMe)_{18}^-$ starts most likely from the detachment of $Au_x(SMe)_y$ from the rearranged semiring staple motifs on the new structure (**Au_{25}−Iso1**) in the MS experiments.

On the basis of the BOMD results, we investigate seven possible fragmentation modes starting from **Au_{25}−Iso1** and compute the relative energies of the fragmentation products, as shown in Figure 5. First, two fragmentation modes involving either the direct loss of a Au(SMe) unit from the dimeric staple

dx.doi.org/10.1021/ja404957t | J. Am. Chem. Soc. 2013, 135, 18067−18079

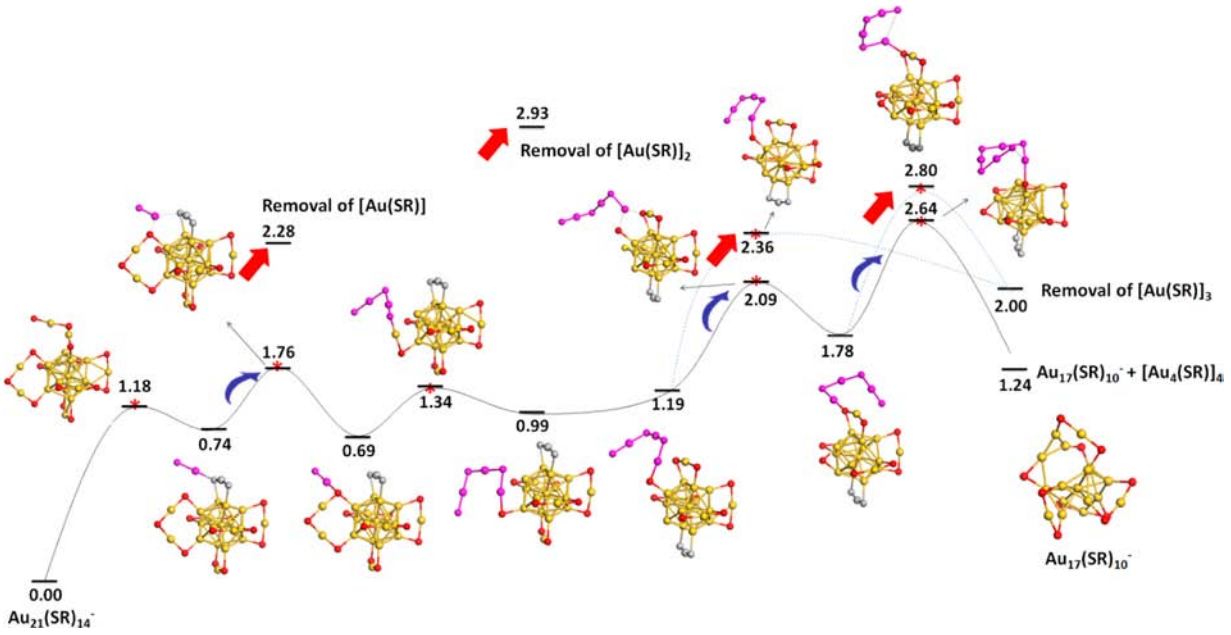

Figure 7. The sequential release of $[Au(SR)]_x$ (x = 1−4) unit from the $Au_{21}(SR)_{14}^-$, where the −R group is simplified into methyl group. The blue arrow indicates a low energy pathway and the red arrow shows a high energy pathway. The atoms colored by pink denote the detached and transferred $[Au(SR)]_x$ units. The atoms in gray denote the formed monomeric staple motifs. Atoms in yellow and red are Au and S, respectively. The relative energies of 82 different isomers of $Au_{17}(SR)_{10}^-$ are displayed in the Supporting Information Figure S3.

motif or the direct detachment of a $Au_2(SMe)_3$ staple motif from **Au_{25}−Iso1** are compared. The products corresponding to the two fragmentation modes are denoted by **FG1** and **FG2**, respectively. As shown in Figure 5, the direct detachment of a $Au_2(SMe)_3$ unit from the cluster is energetically less favorable than the detachment of an Au(SMe) unit. Moreover, Figure 5 shows that the combination of $Au_{21}(SMe)_{14}^-$ and cyclic $Au_4(SMe)_4$ (**FG5**) gives rise to the lowest energy species among various fragmentation products, consistent with the experimental observation of highly popular $Au_{21}(SR)_{14}^-$ and recent theoretical studies.[31] It is worth noting that during each step of $Au_x(SMe)_y$ detachment, the inner Au_{13}-core maintains its quasi-icosahedral structure.

On the basis of the discussions above, a 'step-by-step' fragmentation mechanism of $Au_{25}(SMe)_{18}^-$ toward formation of $Au_{21}(SMe)_{14}^-$ plus a cyclic $[Au(SMe)]_4$, starting from the metastable structure **Au_{25}−Iso1** is proposed. As illustrated in Figure 6, in the first step of the fragmentation, an $Au_2(SMe)_3$ staple motif cleaves one Au-SMe linkage after overcoming an energy barrier of 1.10 eV (**TS1**). This step is consistent with that observed in the high-temperature BOMD simulation discussed above (see Figure 4c). Next, a new metastable isomer structure of $Au_{25}(SMe)_{18}^-$ is formed (denoted as **Au_{25}−Iso2**), in which the middle −SMe− group in the staple motif is linked to the Au-core. This new isomer structure is higher in energy than the **Au_{25}−Iso1** by 0.84 eV. In **Au_{25}−Iso2**, the Au(SMe) unit (colored in pink in Figure 6) dangles on the cluster surface, which can further transfer to a neighboring $Au_2(SMe)_3$ staple motif by overcoming an energy barrier of 0.93 eV. At the end of this transfer process, the Au(SMe) unit attaches to the −SR terminal of a neighboring $Au_2(SMe)_3$ staple motif, leading to the formation of **Au_{25}−Iso3**. Here, we note that the branching pathway that leads to the formation of $Au_{24}(SMe)_{17}^-$ species (**FG2**) represents a higher-energy channel as shown by the red arrow in Figure 6. Continuing from the **Au_{25}−Iso3**, the isomerization of staple motifs further releases an $[Au(SMe)]_2$ unit (**Au_{25}−Iso4**), which can transfer to a neighboring $Au_2(SMe)_3$ staple motif to form **Au_{25}−Iso5**. We find that when the transferred $[Au(SMe)]_x$ species increases to $[Au(SMe)]_3$, the −SR terminal of the dangling $[Au(SMe)]_3$ unit can strongly interact with the attached $Au_2(SMe)_3$ motif (in **Au_{25}−Iso7**) and then leads to the formation of a stable cyclic $[Au(SMe)]_4$ unit and $Au_{21}(SMe)_{14}^-$ (**FG5**). The cyclic $[Au(SMe)]_4$ is too stable to trigger the reactions with additional staple motifs. Moreover, **FG5** also represents a lowest-energy species among various fragment products (**FG1**−**FG5**). From the proposed fragmentation pathway, we also found that other competing pathways for the formation of **FG1**−**FG4** via the direct detachment of $[Au(SMe)]_x$ from the clusters (as marked by the red arrows) are higher energy processes than the transfer of $[Au(SMe)]_x$ unit between two neighboring staple motifs. The transfer of $[Au(SMe)]_x$ units between neighboring staple motifs represents an energetically more favorable pathway, which eventually leads to the formation of $Au_{21}(SMe)_{14}^-$ and a cyclic $[Au(SMe)]_4$, explaining the experimental abundance of $Au_{21}(SR)_{14}^-$ species. Note that the generated $Au_{21}(SMe)_{14}^-$ in **FG5** is a higher energy isomer and has a structural pattern corresponding to **Iso8** described in Figure S1 and Table S1. We suggest that the rearrangement of the staple motifs from $Au_{21}(SMe)_{14}^-$ in **FG5** can eventually lead to the formation of the lowest-energy structure of $Au_{21}(SMe)_{14}^-$ (**Iso1**). The energy profiles for such a structural rearrangement are described in the Supporting Information Figure S2.

Taking the above discussions together, we propose that the formation of $Au_{21}(SR)_{14}^-$ from the fragmentation of $Au_{25}(SR)_{18}^-$ is a stepwise process. The $Au_{25}(SR)_{18}^-$ first transforms into a metastable structure within very short time upon the uptake of energy in the MS. Subsequently, the semiring staple motifs release and stepwise lose a series of $[Au(SR)]_x$ (x = 1−4) units to reach the stable product of $Au_{21}(SR)_{14}^-$ and a cyclic $[Au(SR)]_4$. This stepwise fragmentation mechanism is consistent with previous experimental

dx.doi.org/10.1021/ja404957t | J. Am. Chem. Soc. 2013, 135, 18067−18079

speculations that the cleavage of interfacial Au−S bond and the rearrangement happens during the fragmentation of $Au_{25}(SR)_{18}^-$.[23] In both ESI and MALDI experiments of $Au_{25}(SR)_{18}^-$, the $Au_{21}(SR)_{14}^-$ is a major product due to the favorable cleavage of the Au−S bond.[24,27,28] In particular, the recent IM-MS fragmentation of $Au_{25}(SR)_{18}^-$ clearly showed favorable formation of the $Au_{21}(SR)_{14}^-$ cluster when the cleavage of Au−S bond prevails over other fragmentation modes.[23] In contrast, the formation of $Au_{21}(SR)_{14}^-$ competes with the cleavage of C−S bond in FAB analysis of Au_{25}.[21] Herein, we also note that the superatom electron shell model was commonly used to explain the exceptional stability of $Au_{21}(SR)_{14}^-$. However, there are several fragment clusters such as $Au_{24}(SR)_{17}^-$, $Au_{23}(SR)_{16}^-$ and $Au_{22}(SR)_{15}^-$ that also have the same 8*e* electron shell. In the present study, we offer an alternative viewpoint where the popular formation of $Au_{21}(SR)_{14}^-$ in the MS detection of $Au_{25}(SR)_{18}^-$ is due to not only the underlying thermodynamically favorable process, but also the complicated 'step-by-step' fragmentation mechanism of the interfacial semiring staple motifs.

To further elaborate the proposed stepwise fragmentation mechanism, the continued fragmentation of the $Au_{21}(SR)_{14}^-$ to $Au_{17}(SR)_{10}^-$ is investigated as well. The $Au_{17}(SR)_{10}^-$ is the next principal species in the IM-MS of $Au_{25}(SR)_{18}^-$,[23] which coincides with the further loss of a $[Au(SR)]_4$ unit from $Au_{21}(SR)_{14}^-$. A plausible fragmentation mechanism was proposed by Dass et al. where an rearrangement of the semiring staple motifs on the $Au_{25}(SR)_{18}^-$ nanocluster led to the formation of the $[Au(SR)]_4$ moiety before it fragmented from the cluster.[23] The $Au_{21}(SR)_{14}^-$ can undergo a further intramolecular rearrangement to eliminate another $[Au(SR)]_4$ moiety to form $Au_{17}(SR)_{10}^-$ species under higher collision energies. However, the further fragmentation of the $Au_{17}(SR)_{10}^-$ species involves the Au_{13}-core fragmentation. The whole fragmentation of $Au_{25}(SR)_{18}^-$ has been denoted by a stepped process with the increase of the collision energies,[23] i.e., $[Au_{25}(SR)_{18}^-] \rightarrow [Au_{21}(SR)_{14}^-] + [Au(SR)]_4 \rightarrow [Au_{17}(SR)_{10}^-] + [Au(SR)]_4 \rightarrow Au_{13}$-core fragments, where the $Au_{21}(SR)_{14}^-$, $Au_{17}(SR)_{10}^-$ and $Au_m(SR)_n^-$ are the dominated fragment clusters during the different courses of fragmentation.

Figure 7 displays the continued fragmentation process of the $Au_{21}(SMe)_{14}^-$ to $Au_{17}(SMe)_{10}^-$. We note that the fragmentation steps displayed are essentially the same as those of $Au_{25}(SMe)_{18}^-$ discussed above. In the first two steps, the two dimeric staple motifs can dissociate one Au−S bond, and then a $[Au(SMe)]_x$ (x = 1 or 2) unit transfers to a neighboring staple motif. After the fragmentation of two dimeric staple motifs, the Au_{13}-core is covered by six monomeric staple motifs with a dangling $[Au(SMe)]_2$ unit. In the next step, the cleavage of Au−S bond in a monomeric staple motif entails an energy barrier of 0.9 eV to form a dangling $[Au(SMe)]_3$ unit. After transferring the $[Au(SMe)]_3$ unit to a neighboring mononeric staple motif, the S-terminal of the dangling $[Au(SMe)]_3$ unit can attack the Au(I) atom in the monomeric staple to form a stable $[Au(SMe)]_4$ species and the $Au_{17}(SR)_{10}^-$ is generated. As a comparison, we also investigated the branching fragmentation pathways that lead to the formation of fragmentation products such as $Au_{20}(SMe)_{13}^-$ plus a Au(SMe), $Au_{19}(SMe)_{12}^-$ plus a $[Au(SMe)]_2$, and $Au_{18}(SR)_{11}^-$ plus a $[Au(SR)]_3$, which all turn out to be higher energy processes, indicating the formation of $Au_{17}(SMe)_{10}^-$ and a cyclic $[Au(SMe)]_4$ is also a kinetically controlled process. On the other hand, we find that the remaining single −SR groups caused by the cleavage of Au−S bond in the monomeric staple motifs induce significant distortions of the Au_{13}-core in $Au_{17}(SMe)_{10}^-$. Some Au-core atoms have been lifted by the −SMe groups to form new staple motifs. Our extensive search of the global-minimum structure of $Au_{17}(SMe)_{10}^-$ confirms that the icosahedral Au_{13}-core no longer exists stably (see Figure S3 in the Supporting Information), consistent with the recent IM-MS experiment where the fragmentation of Au_{13}-core occurs after the formation of $Au_{17}(SR)_{10}^-$.[23] Herein, we note that the other fragmentation modes involving the competitive cleavage of C−S bond that lead to fragment species such as $Au_{21}(SR)_{12}S_2^-$ and $Au_{21}(SR)_{10}S_4^-$ (belonging to $[Au_{21}L_{14}^-]$) and $Au_{17}(SR)_8S_2^-$ and $Au_{17}(SR)_6S_4^-$ (belonging to $[Au_{17}L_{10}^-]$)[23] are not discussed in present studies. We focus mainly on the fragmentation mode of the Au−S bond cleavage in the semiring staple motifs.

In summary, the energy profiles shown in Figures 6 and 7 indicate that the fragmentation of $Au_{25}(SMe)_{18}^-$ to $Au_{21}(SMe)_{14}^-$ and then to the $Au_{17}(SMe)_{10}^-$ is an energy increasing process. Moreover, the fragmentation products such as $Au_{21}(SMe)_{14}^-$ plus a cyclic $[Au(SMe)]_4$ species and $Au_{17}(SMe)_{10}^-$ plus two cyclic $[Au(SMe)]_4$ are both thermodynamically less stable than the parent Au_{25} cluster. This conclusion is consistent with the recent MS observations[23] that the fragmentation of semiring staple motifs is prior to the inner Au-core with gradual increase of the collision energy. At lower collision energies, the $Au_{21}(SR)_{14}^-$ is a dominated fragment product, which is further fragmented into $Au_{17}(SR)_{10}^-$ and then the fragmentation of the inner Au_{13}-core happens with the increase of the collision energy. The demonstrated formation mechanism and relative stability of $Au_{21}(SR)_{14}^-$ also suggest that the direct synthesis of Au_{21} cluster via either the wetting chemistry method or the direct heating of Au_{25} cluster is quite difficult because of its low thermodynamic stability and unique formation mechanism. For example, the formation of dimeric staple motifs would be more favorable on an icosahedron Au_{13}-core than the monomeric ones. The Au_{21} cluster with the surface being covered mostly by the monomeric staple motifs might be an intermediate cluster during the bottom-to-up synthesis of $Au_{25}(SR)_{18}^-$ via wetting chemistry method.

3. Mechanism of Selective Oxidation of Styrene on Thiolated-Gold Clusters: A Benchmark Study Based on $Au_{25}(SR)_{18}$ and $Au_{21}(SR)_{14}$. Finally, using $Au_{21}(SR)_{14}$ and its parent Au_{25} cluster as the benchmark model systems, we investigate the possible mechanism of styrene oxidation on thiolated protected gold clusters. The catalytic properties of bare gold clusters have been intensively studied.[52−56] It is well established that 'naked' low-coordinated gold atoms on bare gold clusters provided the major active sites for catalytic reactions. Recently, Jin et al. reported that the thiolate-protected gold clusters such as $Au_{25}(SR)_{18}$, $Au_{38}(SR)_{24}$ and $Au_{144}(SR)_{60}$ exhibit catalytic activities toward several reactions including selected oxidation of styrene and CO oxidation, although the Au-core is protected by the thiolate ligands.[57,58] The experiment results show that the thiolate-protected gold clusters can catalyze styrene into benzaldehyde, styrene epoxide, and acetophenone in the presence of TBHP (*tert*-butyl hydroperoxide) or O_2 with the TBHP as an initiator. In particular, the catalytic reaction exhibits very high selectivity toward the formation of benzaldehyde. However, the underlying mechanism for their catalytic activity is unclear yet. A most controversial question on the catalytic properties of

dx.doi.org/10.1021/ja404957t | J. Am. Chem. Soc. 2013, 135, 18067−18079

thiolate gold clusters is the location of active site on such ligand protected gold clusters. As all gold atoms in the clusters have been either protected by staple motifs or binding with the −SR groups, where is the active site for O_2 activation on these gold clusters? A scenario which has been proposed is that the negatively charged Au-core in thiolated protected gold clusters behaved as the major active sites to activate O_2.[57] Nonetheless, recent theoretical studies indicated the gold atoms in thiolated gold cluster interact weakly with O_2 molecule irrespective of the cluster sizes.[59] The O_2 can be activated by the Au-core only when the surface staple motifs are removed.

Here, we investigate possible active sites and reaction routes for the styrene oxidation on neutral $Au_{21}(SMe)_{14}$ (**Iso1** in Figure 3) and $Au_{25}(SMe)_{18}$. As the O_2 activation is the key step to the styrene oxidation, we first focus on adsorption behavior of O_2 on $Au_{25}(SMe)_{18}$ and $Au_{21}(SMe)_{14}$. As a comparison, the adsorption of O_2 on other thiolated gold clusters with different sizes and charge states, such as $Au_{25}(SMe)_{18}^{0,-1}$, $Au_{38}(SMe)_{24}$, and $Au_{144}(SMe)_{60}$, are examined as well. We find that the interaction between O_2 and various thiolated-gold clusters is rather weak: the O_2 molecule keeps staying away from the clusters' surface after DFT geometric optimization, indicating that the O_2 molecule cannot be effectively adsorbed on the surface of the clusters regardless of the clusters' size and binding sites, consistent with recent theoretical studies.[59]

Next, the adsorption of the styrene on $Au_{25}(SMe)_{18}$ and $Au_{21}(SMe)_{14}$ is examined as well. Again, we find that the styrene cannot be adsorbed on the semiring staple motifs or Au-core. These calculation results suggest that the thiolate protected gold clusters are largely inert toward the adsorption and activation of both O_2 and styrene molecules. In fact, previous experimental studies indicated that the styrene oxidation on thiolated gold clusters is inefficient if only O_2 is provided as the oxidant.[57a] The styrene oxidation became much more efficient on the thiolated gold clusters if the *tert*-butyl hydroperoxide (TBHP) was introduced as the oxidant or initiator. On the basis of the experimental observations, we propose two reaction mechanisms to understand the styrene oxidation on $Au_{25}(SMe)_{18}$ and $Au_{21}(SMe)_{14}$ with either the TBHP or O_2 as the major oxidant: ***Mechanism 1***, the TBHP acts as the sole oxidant, where the O−O bond in TBHP can break hemolytically so as to trigger the reaction; ***Mechanism 2***, the TBHP acts as an initiator and O_2 as the major oxidant, where the −OH group produced from the TBHP activation acts as the cocatalyst. The energy profiles of both mechanisms are illustrated in Figures 8 and 9. We note that both routes have been studied in recent experiments and the styrene can be efficiently converted into benzaldehyde with >90% selectivity at evaluated temperature (~350 K).[57a]

Mechanism 1. The TBHP is the major oxidant. It is well-known the O−O bond in TBHP is very active and the hemolytic cleavage of O−O bond to form the $(CCH_3)O\cdot$ and $OH\cdot$ radicals is the initial activation step under heating. We therefore consider the TBHP first decomposes on the clusters. As shown in Figure 8a, the O−O bond can break on the Au(I) atom in either the monomeric or dimeric staple motif by overcoming an energy barrier of 0.90 or 0.91 eV (**Re** → **Im1**) on $Au_{21}(SMe)_{14}$ or $Au_{25}(SMe)_{18}$, respectively. In the end of this process, the formed $(CCH_3)O\cdot$ and $OH\cdot$ radicals bind strongly to the Au(I) site with energy release of 0.73 or 0.60 eV, respectively. Upon the binding of $(CCH_3)O\cdot$ and $OH\cdot$ radicals, the Au atom in the staple motifs becomes Au(III) (**Im1**). The $(CCH_3)O\cdot$ can further fetch one H atom (**TS1**) from another

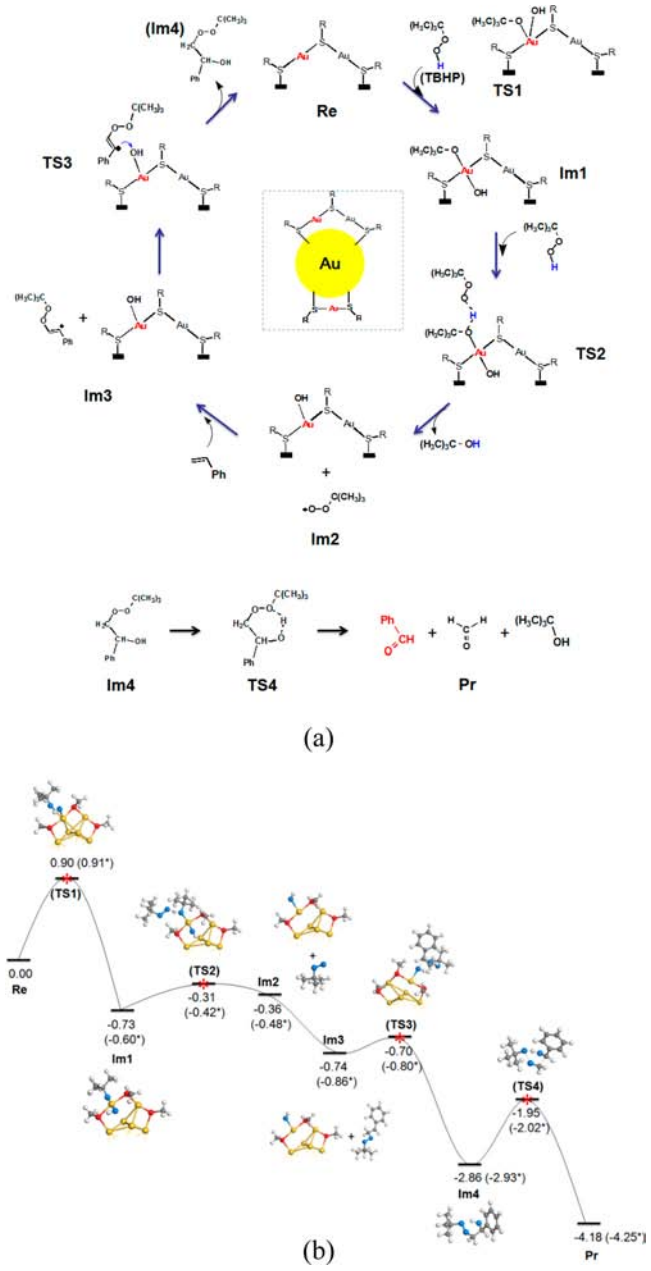

Figure 8. (a) The proposed reaction route of styrene oxidation with the TBHP as the sole oxidant. (b) The computed energy profiles and snapshots of intermediates and transition states on a dimeric motif of $Au_{25}(SMe)_{18}$ based on proposed mechanism. The energies (in unit of eV) are computed at the PBE/DND level. *The energies in each reaction steps of styrene oxidation on a dimeric staple motifs of $Au_{25}(SMe)_{18}$. The snapshots for the reaction intermediates and transition states on the $Au_{21}(SMe)_{14}$ are shown in the Supporting Information as Figure S3. The reaction pathway is computed using the combination of linear synchronous transit (LST)/quadratic synchronous transit (QST) algorithm with conjugated gradient optimization implemented in Dmol[3].

TBHP molecule in the gas phase to form a *tert*-butanol with a energy barrier of 0.42 or 0.18 eV according to the gas-phase mechanism of TBHP activation.[60,61] A $(CCH_3)OO\cdot$ unit is formed, which can further attach to the αC of gas-phase styrene molecule to form a $(CCH_3)OO\text{-}CH_2\text{-}CH\text{-}Ph$ species, included in the **Im3**. The radical center in $(CCH_3)OO\text{-}CH_2\text{-}CH\text{-}Ph$ species can readily fetch the −OH group (**TS3**) on the staple

dx.doi.org/10.1021/ja404957t | J. Am. Chem. Soc. 2013, 135, 18067−18079

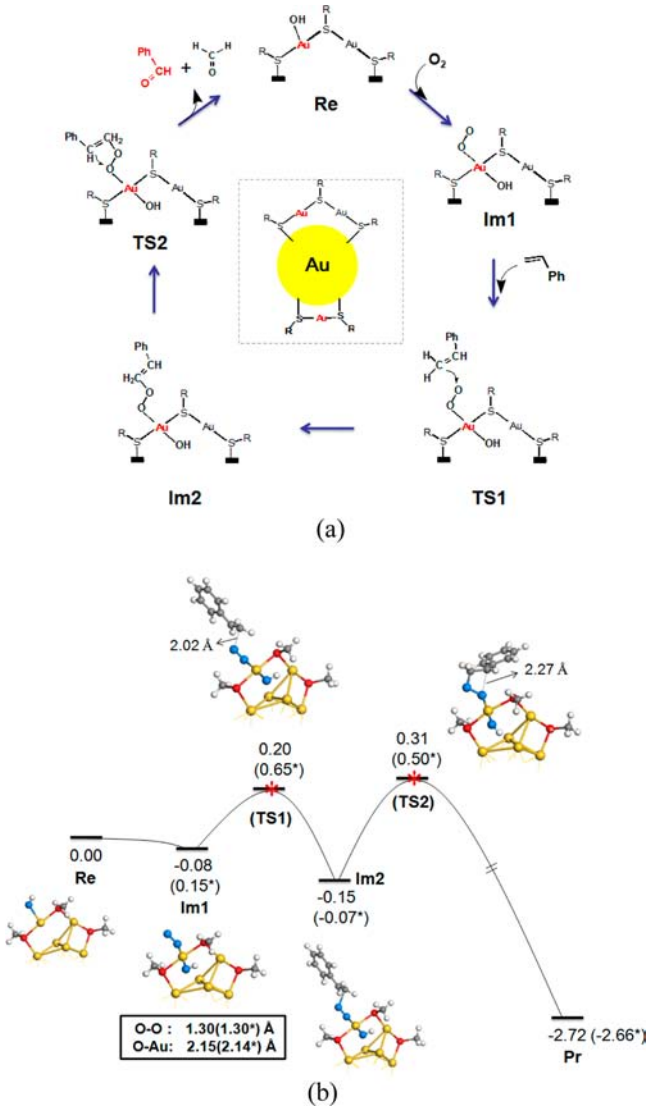

Figure 9. (a) Proposed reaction routes of styrene oxidation with O_2 as the major oxidant and the TBHP as the initiator. Here we assume that the TBHP dissociated on the Au(I) site. (b) The computed energy profiles and snapshots of intermediates and transition states on a dimeric motif of $Au_{25}(SMe)_{18}$ based on proposed mechanism. The energies (in unit of eV) are computed at the PBE/DND level. The reaction pathway is computed using the combination of linear synchronous transit (LST)/quadratic synchronous transit (QST) algorithm with conjugated gradient optimization implemented in Dmol[3]. The snapshots for the reaction intermediates and transition states on the $Au_{21}(SMe)_{14}$ are shown in the Supporting Information as Figure S3. *The energies in each reaction steps of styrene oxidation on a dimeric staple motifs of $Au_{25}(SMe)_{18}$.

motif to form a much stronger C−OH bond in the $(CCH_3)OO$-CH_2-CH(OH)-Ph species (**Im4**), which leads to a large energy release (2.12 or 2.07 eV on $Au_{21}(SMe)_{14}$ and $Au_{25}(SMe)_{18}$, respectively). At the end of this step, the Au_{21} and Au_{25} catalysts are recovered. The gas phase $(CCH_3)OO$-CH_2-CH(OH)-Ph species further decomposes into aldehyde, benzaldehyde, and a *tert*-butanol molecules (**Pr**) to finish the whole catalytic cycle via a transition state structure involving the concerted breaks of C−C, O−O bonds and the transfer of a H atom. The energy barrier in this step is 0.91 eV (**TS4**).

Mechanism 2. If O_2 acts as the major oxidant with small amount of TBHP added as an initiator, the key reaction step involves the activation of styrene or O_2. Our above DFT calculations have shown that both styrene and O_2 molecules interact weakly with the thiolated gold clusters. Thus, it is important to understand how styrene or O_2 is activated on the cluster. In mechanism 2, we propose that the hydroxyl group (−OH) formed from the initial decomposition of TBHP molecule plays a key role during styrene oxidation on thiolated gold clusters. From Figure 9, we find that when the −OH group is preattached to the Au(I) site, the O_2 molecule can bind to the Au(I) site through the formation of an Au−O linkage (**Re** → **Im1**). From Figure 9, the bond length of Au−O linkage on the $Au_{21}(SMe)_{14}$ and $Au_{25}(SMe)_{18}$ is 2.15 and 2.14 Å, respectively. Although the binding energy of O_2 is small, we find that the O−O bond is elongated to 1.30 Å on both clusters, much longer than that in the gas phase (1.24 Å). Most importantly, the O_2 molecule is stably bound at the Au(I) site, in contrast to the interaction styles on the clusters without −OH preadsorption described above. We find that the bound O_2 molecule may undergo further activation by the attack of gas-phase styrene molecule. The attack of αC in styrene to the O_2 leads to form a C−O bond described by **Im2** in Figure 9. The energy barrier in this step is 0.28 and 0.50 eV on $Au_{21}(SMe)_{14}$ and $Au_{25}(SMe)_{18}$ (**TS1**), respectively. In the **Im2**, the βC in the styrene specie demonstrates radical characters, which can further attack the bottom O atom to break the O−O bond to form the final products such as benzaldehyde and aldehyde. The energy barrier in this step (**Im2** → **Pr**) is 0.46 and 0.57 eV on $Au_{21}(SMe)_{14}$ and $Au_{25}(SMe)_{18}$, respectively.

In light of the two proposed mechanisms, we find that the Au(I) site in the semiring staple motifs on both $Au_{25}(SMe)_{18}$ and $Au_{21}(SMe)_{14}$ is the major active site toward styrene oxidation rather than the inner metallic Au-core. The fundamental mechanism for the activation mechanism of O_2 on the Au(I) site is attributed to the preadsorbed −OH group at the Au(I) site. Upon the adsorption of O_2, the gold atom in the staple motifs forms tetra-coordinated Au(III) structure. The O_2 is activated on the Au-atom in this step as demonstrated in mechanism 2 (Figure 9). This mechanism indicates the transition of Au-atom in the semiring staple motifs from Au(I) to Au(III) is a key for the O_2 activation and styrene oxidation on thiolate protected gold clusters. We note that the current proposed reaction mechanism and active site would be valid for $Au_{25}(SMe)_{18}$ and $Au_{21}(SMe)_{14}$, which can also be extended to understand the catalytic activity of other thiolate protected gold clusters such as $Au_{38}(SR)_{24}$ as long as the unique semiring staple motifs are present on those clusters.

■ CONCLUSION

In sum, the fragmentation mechanism and catalytic active site of the $Au_{25}(SR)_{18}$ cluster are investigated using density functional theory (DFT) calculations. The atomic structure of $Au_{21}(SR)_{14}^{-}$, a magic fragmentation product of $Au_{25}(SR)_{18}^{-}$, is predicted on basis of our recent developed force-field based 'divide-and-protect' approach. Our extensive structural searches suggest that the $Au_{21}(SR)_{14}^{-}$ cluster contains a quasi-icosahedra Au_{13}-core with four monomeric *-SR-Au-SR-* and two dimeric *-SR-Au-SR-Au-SR-* semiring staple motifs. A stepwise fragmentation pathway of the semiring staple motifs on the $Au_{25}(SR)_{18}^{-}$ is proposed. We show that the $Au_{25}(SR)_{18}^{-}$ can first transform into a metastable structure with all staple motifs binding to two neighboring vertex Au-atoms of Au-core upon energy uptake, followed by 'step-by-step' detachment and transfer of a series of $[Au(SR)]_x$ (x = 1−4) units from the metastable structure to

dx.doi.org/10.1021/ja404957t | J. Am. Chem. Soc. 2013, 135, 18067−18079

reach the $Au_{21}(SR)_{14}^-$ cluster. Together with the computed relative energies of various fragmentation products, intermediates and transition states during the fragmentation processes, the favorable formation of $Au_{21}(SR)_{14}^-$ and a cyclic $[Au(SR)]_4$ is not only attributed to the underlying thermodynamically favorable process, but also controlled by the complicated stepwise fragmentation mechanism. The continue fragmentation of $Au_{21}(SR)_{14}^-$ to $Au_{17}(SR)_{10}^-$ is observed as well, which has the same stepwise fragmentation mechanism as their parent Au_{25} cluster. The present studies of the fragmentation mechanism of semiring staple motifs together with our recent theoretical studies of the structure of magic $Au_mS_n^-$ clusters[29] caused by the fragmentation of inner Au_{13}-core of $Au_{25}(SR)_{18}^-$ provide a comprehensive understanding of the fragmentation behaviors of $Au_{25}(SR)_{18}^-$ cluster in MS.

Finally, using the predicted structure of $Au_{21}(SR)_{14}$ and its parent cluster $Au_{25}(SR)_{18}$ as the benchmark systems, we find that the Au(I) site in the semiring staple motifs can also act as the major active site for the catalytic oxidation of styrene. The Au atom in the staple motifs can change its valence state from Au(I) and Au(III) upon O_2 adsorption, which is considered a key step for the activation of O_2 molecules. The proposed reaction mechanism may be extended to other thiolate protected gold clusters provided the presence of wrapped staple motifs on the cluster surfaces.

■ ASSOCIATED CONTENT

Supporting Information

Computed UV−vis absorption spectra for **Iso1−16**, the relative and absolute electronic energies of isomer structures of $Au_{21}(SMe)_{14}$, the relative energies of isomers of $Au_{17}(SMe)_{10}^-$, the snapshots of reaction intermediate, transition states of styrene oxidation on $Au_{21}(SMe)_{14}$, a transformation mechanism between two isomers of $Au_{21}(SMe)_{14}$, and the coordinates of **Iso1−3** and **Iso9−10** are provided. This material is available free of charge via the Internet at http://pubs.acs.org.

■ AUTHOR INFORMATION

Corresponding Author

ypnku78@gmail.com

Notes

The authors declare no competing financial interest.

■ ACKNOWLEDGMENTS

Y.P. is supported by Natural Science Foundation of China (Grant No. 21103144 and 21373176), Hunan Provincial Natural Science Foundation of China (12JJ7002, 12JJ1003), Scientific Research Fund of Hunan Provincial Education Department (13A100). X.C.Z. is supported by grants from the NSF (EPS-1010674), ARL (W911NF1020099), and the Nebraska Research Initiative, and by University of Nebraska's Holland Computing Center and the Center for Functional Nanomaterials (CFN) Theory and Computation Facility in Brookhaven National Laboratory (research carried out in part at the Center for Functional Nanomaterials, Brookhaven National Laboratory, which is supported by the U.S. Department of Energy, Office of Basic Energy Sciences, under Contract No. DE-AC02-98CH10886).

■ REFERENCES

(1) (a) Whetten, R. L.; Khoury, J. T.; Alvarez, M. M.; Murthy, S.; Vezmar, I.; Wang, Z. L.; Stephens, P. W.; Cleveland, C. L.; Luedtke, W. D.; Landman, U. *Adv. Mater.* **1996**, *8*, 428. (b) Schaaff, T. G.; Shafigullin, M. N.; Khoury, J. T.; Vezmar, K. I.; Whetten, R.; Gullen, W. G.; First, P. N. *J. Phys. Chem. B* **1997**, *101*, 7885. (c) Chen, S.; Ingram, R. S.; Hostetler, M. J.; Pietron, J. J.; Murray, R. W.; Schaaff, T. G.; Khoury, J. T.; Alvarez, M. M.; Whetten, R. L. *Science* **1998**, *280*, 2098. (d) Templeton, A. C.; Wuelfing, W. P.; Murray, R. W. *Acc. Chem. Res.* **2000**, *33*, 27. (e) Sardart, R.; Funston, A. M.; Mulvaney, P.; Murray, R. W. *Langmuir* **2009**, *25*, 13840. (f) Price, R. C.; Whetten, R. L. *J. Am. Chem. Soc.* **2005**, *127*, 13750. (g) Parker, J. F.; Fields-Zinna, C. A.; Murray, R. W. *Acc. Chem. Res.* **2010**, *43*, 1289.

(2) (a) Tsunoyama, H.; Nickut, P.; Negishi, Y.; Al-Shamery, K.; Matsumoto, Y.; Tsukuda, T. *J. Phys. Chem. C* **2007**, *111*, 4153. (b) Chaki, N. K.; Tsunoyama, H.; Negishi, Y.; Sakurai, H.; Tsukuda, T. *J. Phys. Chem. C* **2007**, *111*, 4885. (c) Tsunoyama, H.; Sakurai, H.; Negishi, Y.; Tsukuda, T. *J. Am. Chem. Soc.* **2005**, *127*, 9374. (d) Tsunoyama, H.; Sakurai, H.; Tsukuda, T. *Chem. Phys. Lett.* **2006**, *429*, 528. (e) Liu, Y.; Tsunoyama, H.; Akita, T.; Tsukuda, T. *Chem. Commun.* **2010**, *46*, 550. (f) Liu, Y.; Tsunoyama, H.; Akita, T.; Xie, S.; Tsukuda, T. *ACS Catal.* **2011**, *1*, 2.

(3) Lopez-Acevedo, O.; Kacprzak, K. A.; Akola, J.; Häkkinen, H. *Nat. Chem.* **2010**, *2*, 329.

(4) Huang, X.; El-Sayed, I. H.; Qian, W.; El-Sayed, M. A. *J. Am. Chem. Soc.* **2006**, *128*, 2115.

(5) Cao, Y. C.; Jin, R.; Nam, J.; Thaxton, C. S.; Mirkin, C. A. *J. Am. Chem. Soc.* **2003**, *125*, 14676.

(6) (a) Jin, R. *Nanoscale* **2010**, *2*, 343. (b) Zhu, Y.; Qian, H.; Drake, B. A.; Jin, R. *Angew. Chem., Int. Ed.* **2010**, *49*, 1295. (c) Zhu, Y.; Qian, H.; Zhu, M.; Jin, R. *Adv. Mater.* **2010**, *22*, 1915. (d) Zhu, Y.; Wu, Z.; Cayathri, G. C.; Qian, H.; Gil, R. R.; Jin, R. *J. Catal.* **2010**, *271*, 155.

(7) Jadzinsky, P. D.; Calero, G.; Ackerson, C. J.; Bushnell, D. A.; Kornberg, R. D. *Science* **2007**, *318*, 430.

(8) Heaven, M. W.; Dass, A.; White, P. S.; Holt, K. M.; Murray, R. W. *J. Am. Chem. Soc.* **2008**, *130*, 3754.

(9) (a) Qian, H.; Jin, R. *Nano Lett.* **2009**, *9*, 4083. (b) Zhu, M.; Qian, H.; Jin, R. *J. Am. Chem. Soc.* **2009**, *131*, 7220. (c) Zhu, M.; Qian, H.; Jin, R. *J. Phys. Chem. Lett.* **2010**, *1*, 1003. (d) Jin, R.; Qian, H.; Wu, Z.; Zhu, Y.; Zhu, M.; Mohanty, A.; Garg, N. *J. Phys. Chem. Lett.* **2010**, *1*, 2903. (e) Qian, H.; Jin, R. *Chem. Mater.* **2011**, *23*, 2209. (f) Qian, H.; Zhu, Y.; Jin, R. *J. Am. Chem. Soc.* **2010**, *132*, 4583. (g) Qian, H.; Eckenhoff, W. T.; Zhu, Y.; Pintauer, T.; Jin, R. *J. Am. Chem. Soc.* **2010**, *132*, 8280. (h) Wu, Z.; MacDonald, M. A.; Chen, J.; Zhang, P.; Jin, R. *J. Am. Chem. Soc.* **2011**, *133*, 9670. (i) Qian, H.; Zhu, Y.; Jin, R. *Proc. Natl. Acad. Sci. U.S.A.* **2012**, *109*, 696. (j) Zeng, C.; Qian, H.; Li, T.; Li, G.; Rosi, N.; Yoon, B.; Whetten, R.; Landman, U.; Jin, R. *Angew. Chem., Int. Ed.* **2012**, *51*, 13114. (k) Zhu, M.; Aikens, C. M.; Hollander, F. J.; Schatz, G. C.; Jin, R. *J. Am. Chem. Soc.* **2008**, *130*, 5883. (l) Zeng, C.; Li, T.; Das, A.; Rosi, N. L.; Jin, R. *J. Am. Chem. Soc.* **2013**, *135*, 10011.

(10) Negishi, Y.; Takasugi, Y.; Sato, S.; Yao, H.; Kimura, K.; Tsukuda, T. *J. Am. Chem. Soc.* **2004**, *126*, 6518.

(11) Schaaff, T. G.; Whetten, R. L. *J. Phys. Chem. B* **2000**, *104*, 2630.

(12) (a) Ramakrishna, G.; Varnavski, O.; Kim, J.; Lee, D.; Goodson, T. *J. Am. Chem. Soc.* **2008**, *130*, 5032. (b) Varnavski, O.; Ramakrishna, G.; Kim, J.; Lee, D.; Goodson, T. *J. Am. Chem. Soc.* **2010**, *132*, 16.

(13) Price, R. C.; Whetten, R. L. *J. Am. Chem. Soc.* **2005**, *127*, 13750.

(14) Nimmala, P. R.; Dass, A. *J. Am. Chem. Soc.* **2011**, *133*, 9175.

(15) Wang, Z. W.; Toikkanen, O.; Yin, F.; Li, Z. Y.; Quinn, B. M.; Palmer, R. E. *J. Am. Chem. Soc.* **2010**, *132*, 2854.

(16) (a) Pei, Y.; Zeng, X. C. *Nanoscale* **2012**, *4*, 4054. (b) Jiang, D. *Nanoscale* **2013**, *5*, 7149.

(17) (a) Jiang, D.; Whetten, R. L.; Luo, W.; Dai, S. *J. Phys. Chem. C* **2009**, *113*, 17291. (b) Jiang, D. *Chem.—Eur. J.* **2011**, *17*, 12289. (c) Jiang, D.; Chen, W.; Whetten, R. L.; Chen, Z. *J. Phys. Chem. C* **2009**, *113*, 16983. (d) Jiang, D.; Tiago, M. L.; Luo, W.; Dai, S. *J. Am. Chem. Soc.* **2008**, *130*, 2777. (e) Jiang, D.; Overbury, S. H.; Dai, S.. *J. Am. Chem. Soc.* **2013**, *135*, 8786. (f) Jiang, D.; Walter, M.; Akola, J. *J. Phys. Chem. C* **2010**, *114*, 15883.

(18) (a) Tlahuice-Flores, A.; Garzón, I. L. *Phys. Chem. Chem. Phys.* **2012**, *14*, 3737. (b) Tlahuice-Flores, A.; Jose-Yacamán, M.; Whetten, R. L. *Phys. Chem. Chem. Phys.* **2013**, *15*, 19557.
(19) (a) Pei, Y.; Gao, Y.; Shao, N.; Zeng, X. C. *J. Am. Chem. Soc.* **2009**, *131*, 13619. (b) Pei, Y.; Pal, R.; Liu, C.; Gao, Y.; Zhang, Z.; Zeng, X. C. *J. Am. Chem. Soc* **2012**, *134*, 3015. (c) Pei, Y.; Gao, Y.; Zeng, X. C. *J. Am. Chem. Soc.* **2008**, *130*, 7830.
(20) (a) Häkkinen, H.; Walter, M.; Grönbeck, H. *J. Phys. Chem. B* **2006**, *110*, 9927. (b) Lopez-Acevedo, O.; Tsunoyama, H.; Tsukuda, T.; Häkkinen, H.; Aikens, C. M. *J. Am. Chem. Soc.* **2010**, *132*, 8210. (c) Lopez-Acevedo, O.; Akola, J.; Whetten, R. L.; Grönbeck, H.; Häkkinen, H. *J. Phys. Chem. C* **2009**, *113*, 5305. (d) Akola, J.; Walter, M.; Whetten, R. L.; Häkkinen, H.; Grönbeck, H. *J. Am. Chem. Soc* **2008**, *130*, 3756.
(21) Dass, A.; Dubay, G. R.; Fields-Zinna, C. A.; Murray, R. W. *Anal. Chem.* **2008**, *80*, 6845.
(22) Schaaff, T. G.; Shafigullin, M. N.; Khoury, J. T.; Vezmar, I.; Whetten, R. L. *J. Phys. Chem. B* **2001**, *105*, 8785.
(23) Angel, L. A.; Majors, L. T.; Dharmaratne, A. C.; Dass, A. *ACS Nano* **2010**, *4*, 4691.
(24) Fields-Zinna, C. A.; Sampson, J. S.; Crowe, M. C.; Tracy, J. B.; Parker, J. F.; deNey, A. M.; Muddiman, D. C.; Murray, R. W. *J. Am. Chem. Soc.* **2009**, *131*, 13844.
(25) Negishi, Y.; Takasugi, Y.; Sato, S.; Yao, H.; Kimura, K.; Tsukuda, T. *J. Phys. Chem. B* **2006**, *110*, 12218.
(26) Shichibu, Y.; Negishi, Y.; Tsukuda, T.; Teranishi, T. *J. Am. Chem. Soc.* **2005**, *127*, 13464.
(27) Qian, H.; Barry, E.; Zhu, Y.; Jin, R. *Acta Phys. Chim. Sin.* **2011**, *27*, 513.
(28) Dass, A.; Stevenson, A.; Dubay, G. R.; Tracy, J. B.; Murray, R. W. *J. Am. Chem. Soc.* **2008**, *130*, 5940.
(29) Pei, Y.; Shao, N.; Li, H.; Jiang, D.-E.; Zeng, X. C. *ACS Nano* **2011**, *5*, 1441.
(30) Jiang, D. E.; Walter, S.; Dai, S. *Chem.—Eur. J.* **2010**, *16*, 4999.
(31) Lopez-Acevedo, O.; Häkkinen, H. *Eur. Phys. J. D* **2011**, *63*, 311.
(32) Perdew, J. P.; Burke, K.; Ernzerhof, M. *Phys. Rev. Lett.* **1996**, *77*, 3865.
(33) Staroverov, V. N.; Scuseria, G. E.; Tao, J.; Perdew, J. P. *J. Chem. Phys.* **2003**, *119*, 12129.
(34) (a) Zhao, Y.; Truhlar, D. G. *J. Phys. Chem. A* **2006**, *110*, 13126. (b) Zhao, Y.; Truhlar, D. G. *J. Chem. Phys.* **2006**, *125*, 194101. (c) Mantina, M.; Valero, R.; Truhlar, D. G. *J. Chem. Phys.* **2009**, *131*, 064706.
(35) Delley, B. *J. Chem. Phys.* **1990**, *92*, 508; *J. Chem. Phys.* **2003**, *113*, 7756 $DMol^3$ 4.4 is available from Accelrys..
(36) ADF 2010.01, SCM, Theoretical Chemistry, Vrije Universiteit, Amsterdam, The Netherlands (http://www.scm.com).
(37) *Gaussian 09*, Revision A.1, Frisch, M. J.; et al.et al.; Gaussian, Inc.: Wallingford, CT, 2009. The full citation of Gaussian 09 package is given in the Supporting Information.
(38) van Leeuwen, R.; Baerends, E. J. *Phys. Rev. A* **1994**, *49*, 2421.
(39) Aikens, C. M. *J. Phys. Chem. A* **2009**, *113*, 10811.
(40) Lippert, G.; Hutter, J.; Parrinello, M. *Mol. Phys.* **1997**, *92*, 477.
(41) (a) The CP2K developers group, http://cp2k.berlios.de/, 2004. (b) Goedecker, S.; Teter, M.; Hutter, J. *Phys. Rev. B* **1996**, *54*, 1703.
(42) Hartwigsen, C.; Goedecker, S.; Hutter, J. *Phys. Rev. B* **1998**, *58*, 3641.
(43) Hartke, B. *J. Phys. Chem.* **1993**, *97*, 9973.
(44) Xiang, H.; Wei, S.-H.; Gong, X. *J. Am. Chem. Soc.* **2010**, *132*, 7355.
(45) Kirkpatrick, S.; Gelatt, C. D.; Vecchi, M. P. *Science* **1983**, *220*, 671.
(46) (a) Wales, D. J.; Doye, J. P. K. *J. Phys. Chem. A* **1997**, *101*, 5111. (b) Yoo, S.; Zeng, X. C. *Angew. Chem., Int. Ed.* **2005**, *44*, 1491.
(47) Sutton, A. P.; Chen, J. *Philos. Mag. Lett.* **1990**, *61*, 139.
(48) (a) Head-Gordon, M.; Pople, J. A.; Frisch, M. J. *Chem. Phys. Lett.* **1988**, *153*, 503. (b) Frisch, M. J.; Head-Gordon, M.; Pople, J. A. *Chem. Phys. Lett.* **1990**, *166*, 275. The MP2 single-point energy calculations are performed using the geometric structure that first optimized by TPSS functional.
(49) Zhu, M.; Eckenhoff, W. T.; Pintauer, T.; Jin, R. *J. Phys. Chem. C* **2008**, *112*, 14221.
(50) Walter, M.; Akola, J.; Lopez-Acevedo, O.; Jadzinsky, P. D.; Calero, G.; Ackerson, C. J.; Whetten, R. L.; Grönbeck, H.; Häkkinen, H. *Proc. Natl. Acad. Sci. U.S.A.* **2008**, *105*, 9157.
(51) Private communication with Prof. Rongchao Jin at Carnegie Mellon University and Prof. Challa Kumar at Lousiana State University.
(52) (a) Haruta, M.; Kobayashi, T.; Samo, H.; Yamada, N. *Chem. Lett.* **1987**, *2*, 405. (b) Haruta, M.; Yamada, N.; Kobayashi, T.; Iijima, S. *J. Catal.* **1989**, *115*, 301.
(53) Bailie, J. E.; Hutchings, G. J. *Chem. Commun.* **1999**, *21*, 2151.
(54) Landon, P.; Collier, P. J.; Papworth, A. J.; Kiely, C. J.; Hutchings, G. J. *Chem. Commun.* **2002**, *18*, 2058.
(55) Hughes, M. D.; Xu, Y.; Jenkins, P.; McMorn, P.; Landon, P.; Enache, D. I.; Carley, A. F.; Attard, G. A.; Hutchings, G. J.; King, F.; Stitt, E. H.; Johnston, P.; Griffin, K.; Kiely, C. J. *Nature* **2005**, *437*, 1132.
(56) Fu, Q.; Saltsburg, H.; Flytzani-Stephanopoulos, M. *Science* **2003**, *301*, 935.
(57) (a) Zhu, Y.; Qian, H.; Jin, R. *Chem.—Eur. J.* **2010**, *16*, 11455–11462. (b) Qian, H.; Jiang, D.-E.; Li, G.; Gayathri, C.; Das, A.; Gil, R. R.; Jin, R. *J. Am. Chem. Soc.* **2012**, *134*, 16159. (c) Li, G.; Jin, R. *Acc. Chem. Res.* **2013**, *46*, 1749. (d) Zhu, Y.; Qian, H.; Jin, R. *Adv. Mater.* **2010**, *22*, 1915.
(58) Nie, X.; Qian, H.; Ge, Q.; Xu, H.; Jin, R. *ACS Nano* **2012**, *6*, 6014.
(59) Lopez-Acevedo, O.; Kacprzak, K. A.; Akola, J.; Häkkinen, H. *Nat. Chem.* **2010**, *2*, 329.
(60) (a) Hiatt, R.; Mill, T.; Mayo, F. R. *J. Org. Chem.* **1965**, *33*, 1416. (b) Hiatt, R.; Mill, T.; Irwin, K. C.; Castleman, J. K. *J. Org. Chem.* **1968**, *33*, 1428.
(61) Barton, D. H. R.; Le Gloahec, V. N. *Tetrahedron* **1998**, *54*, 1557.